Full Control of the Polarisation Configuration in Epitaxial Lead Titanate Ferroelectric Ultrathin Films

Weymann, Christian

UNIVERSITÉ DE GENÈVE
Département de Physique
de la Matière Quantique

FACULTÉ DES SCIENCES
Professeure P. Paruch
Professeur J.-M. Triscone

Full Control of the Polarisation Configuration in Epitaxial Lead Titanate Ferroelectric Ultrathin Films

THÈSE

présentée à la Faculté des Sciences de l'Université de Genève pour obtenir le grade de docteur ès Sciences, mention Physique

par

Weymann Christian
de
Genève (GE)

Thèse n° 5423

GENÈVE
Atelier d'impression ReproMail
2019

UNIVERSITÉ DE GENÈVE
FACULTÉ DES SCIENCES

DOCTORAT ÈS SCIENCES, MENTION PHYSIQUE

Thèse de Monsieur Christian WEYMANN

intitulée :

«Full Control of the Polarisation Configuration in Epitaxial Lead Titanate Ferroelectric Ultrathin Films»

La Faculté des sciences, sur le préavis de Madame P. PARUCH, professeure associée et directeur de thèse (Département de physique de la matière quantique), Monsieur J.-M. TRISCONE, professeur ordinaire et codirecteur de thèse (Département de physique de la matière quantique), Monsieur R. CERNY, professeur associé (Laboratoire de cristallographie, section de physique), Monsieur M. TRASSIN, docteur (Department of Materials, Ecole Polytechnique Fédérale de Zürich, Suisse), Monsieur J. HINKA, professeur (Institute of Physics, Academy of Sciences of the Czech Republic, Prague, République Tchèque), autorise l'impression de la présente thèse, sans exprimer d'opinion sur les propositions qui y sont énoncées.

Genève, le 17 décembre 2019

Thèse - 5423 -

Le Doyen

N.B. - La thèse doit porter la déclaration précédente et remplir les conditions énumérées dans les "Informations relatives aux thèses de doctorat à l'Université de Genève".

When you have eliminated the impossible, whatever remains, however improbable, must be the truth.

–*Sherlock Holmes*, in the works of Sir Arthur Conan Doyle

Résumé

Découverts dans les année 1920, les matériaux ferroélectriques se caractérisent par une polarisation électrique dite rémanente, présente en l'absence de champ électrique extérieur, et qui peut, par l'application d'un champ électrique suffisamment élevé, être basculée entre différentes valeurs stables. Par symétrie cristalline, tous les ferroélectriques sont aussi pyrolélectriques, c'est-à-dire que leur polarisation dépend de la température, et piézoélectriques, c'est-à-dire qu'une déformation mécanique induit une polarisation électrique de ces matériaux, et vice-versa. Dès le départ, c'est principalement pour ces deux propriétés que les ferroélectriques sont utilisés dans les applications industrielles, comme les sonars ou les détecteurs infrarouges. La recherche et l'utilisation des ferroélectriques s'est considérablement accélérée à partir des années 1940, après la découverte du premier oxyde ferroélectrique, le titanate de baryum. Ce composé est le premier d'une nouvelle classe de ferroélectriques, présentant une structure stable à conditions ambiantes, un processus de fabrication grandement simplifié, et une structure cristalline suffisamment simple pour faire l'objet d'études théoriques *ab initio*. C'est de cette classe de matériaux qu'est également issu le titanate de plomb, qui est le matériau examiné dans cette thèse.

Comme plusieurs valeurs de polarisation sont stables pour chaque matériau ferroélectrique, il arrive que des polarisations différentes soient présentes dans le même échantillon à différents endroits: on parle alors de domaines. La présence de ces domaines peut fortement influencer les propriétés pyro-, piézo-, et diélectriques d'un échantillon; leur contrôle est dès lors essentiel pour les applications. De plus, ces domaines peuvent servir a stocker de l'information binaire, ce qui ouvre le champ d'application des mémoires informatiques ferroélectriques. Là encore, il est essentiel de maitriser la structure de domaines présente dans les échantillons pour éviter les erreurs de stockage.

Les séparations entre les domaines sont appelées parois de domaine, et

font l'objet d'un intérêt actif de la part de la communauté scientifique. En effet, de nombreuses propriétés absentes à l'intérieur des domaines ont été découvertes aux parois de domaine. L'exemple le plus marquant est sans doute la découverte de parois de domaine conductrices dans des échantillons ferroélectriques isolants, ouvrant des possibilités pour des circuits électriques nanométriques entièrement reconfigurables. De plus, le changement de symétrie à la paroi de domaine en fait un lieu propice à l'apparition d'une structure interne non-triviale. En effet, alors que le consensus était que la polarisation de l'échantillon devait localement aller à zéro en passant d'un domaine à un autre polarisé en sens opposé, de récents travaux théoriques et expérimentaux ont démontré la possibilité pour la polarisation de tourner sur elle-même sans passer par zéro. Ces matériaux peuvent ainsi former des domaines très petits et particulièrement stables, appelés skyrmions.

Il existe de nombreuses méthodes pour contrôler la structure de domaines dans un échantillon, la plus simple étant de le soumettre à un fort champ électrique pour aligner tous les domaines. Les progrès des méthodes de dépositions par vapeur physique de ces dernières décennies ont aussi permis la production d'échantillons avec une structure de domaines intrinsèque contrôlée. En effet, ces méthodes permettent non seulement de produire des échantillons atomiquement plats et de grande cohérence cristalline, mais aussi de précisément maitriser leurs conditions de bords, qui ont une forte influence sur la structure de domaines. Il manque cependant une méthode fiable pour produire des séries d'échantillons identiques en tous points, sauf la structure de domaines intrinsèque.

Dans cette thèse, nous présentons une méthode qui nous permet de répondre à ce besoin: en changeant la température de croissance de nos échantillons, nous contrôlons entièrement la direction de la polarisation et la structure de domaines dans des couches minces de titanate de plomb, comme nous le démontrons par microscopie à force piézoélectrique (PFM). Une analyse détaillée de la stœchiométrie de nos échantillons par spectroscopie de rétrodiffusion de Rutherford (RBS) nous apprend que les échantillons polarisés hors du plan vers le bas ont une plus forte concentration de lacunes de plomb, et que cette concentration augmente proche de la surface. Ceci nous conduit à un modèle microscopique de dipoles de lacunes de plomb et d'oxygène qui se forment pendant le dépôt de l'échantillon, et qui stabilisent sa direction de polarisation préférentielle. Des mesures de diffraction de rayons-x montrent des variations de la taille de la maille unitaire hors du plan, ce que nous connectons à une variation de la valeur de la polarisation induite par les dipoles à l'aide d'un modèle utilisant le formalisme de Ginzburg, Landau, et Devonshire. Ce modèle explique également nos observations en fonction de l'épaisseur de l'échantillon et de la température appliquée *ex-situ*.

La température de croissance est un paramètre d'optimisation important pour le dépôt de nos échantillons, et la fenêtre de température qui

présente une croissance optimale est restreinte. Nous démontrons que par une modification simple de notre technique de dépôt, nous pouvons agrandir considérablement cette fenêtre de température, afin de profiter de l'effet présenté précédemment sans pertes dans la qualité des échantillons. En effet, en interrompant périodiquement le flux de matériau déposé, nous obtenons une augmentation significative de la qualité cristalline, mesurée par diffraction de rayons-x, et de qualité de surface, mesurée par microscopie à force atomique. Nous démontrons en outre que cette technique est applicable à d'autres matériaux que le titanate de plomb.

Finalement, nous présentons nos travaux en cours sur une des applications de ces séries d'échantillons avec une structure de domaines contrôlée. Nous comparons des analyses par microscopie à génération de seconde harmonique (SHG) sur des parois de domaine artificielles, écrites dans un échantillon monodomaine, et des parois intrinsèques, dans un échantillon polydomaine. Les parois écrite se révèlent avoir un polarisation dans le plan, perpendiculaire au plan de la paroi, alors que les parois intrinsèques sont trop proches pour être correctement résolue par notre technique de mesure optique. Néanmoins, ces images montrent un certain contraste, que nous pouvons expliquer par des variations de la densité des domaines. Un modèle d'Ising nous permet en outre de connecter ces variations de densité à la présence de variations spatiale d'un potentiel favorisant une direction de la polarisation. Plus d'analyses sont nécessaires pour en déterminer l'origine, et la structure interne des parois intrinsèques.

Cette thèse nous laisse avec une méthode puissante pour produire des échantillons ferroélectriques de haute qualité, avec un contrôle indépendant de la structure de domaines. Toute étude visant à comparer les effets de domaines intrinsèques à ceux de domaines artificiels pourra en profiter. Ce type de série d'échantillons serait par exemple précieuse pour l'étude de l'influence de la polarisation sur la condensation et la cristallisation de l'eau à la surface de ferroélectriques, où il a déjà été démontré que la structure de la surface et l'histoire d'écriture de l'échantillon ont une influence importante.

Contents

Résumé **i**

1 Introduction **1**

2 Background **5**
2.1 Ferroelectricity 5
2.1.1 Phenomenology 5
2.1.2 Lead titanate, a prototypical oxide ferroelectric 7
2.1.3 Soft modes 8
2.1.4 The modern theory of ferroelectricity and Born effective charge 8
2.2 Domains and domain walls 11
2.2.1 The depolarising field 11
2.2.2 The built-in field 15
2.2.3 Conducting domain walls and domain wall nanoelectronics 17
2.2.4 Non-Ising domain walls and exotic polarisation textures 18

3 Ginzburg-Landau-Devonshire approach to ferroelectrics **21**
3.1 Conjugate variables 21
3.2 Symmetry and physical arguments 22
3.3 Dealing with inhomogeneity: the Ginzburg-Landau theory . . 24
3.4 Applying the constraints of thin film geometry 25

4 Experimental methods **27**
4.1 Scanning probe microscopy 27

4.1.1 Atomic force microscopy . . . 27
4.1.2 Piezoresponse force microscopy . . . 29
4.2 X-ray diffraction . . . 33
4.3 Second Harmonic Generation . . . 38
4.4 Off-axis radio frequency magnetron sputtering . . . 39

5 Effect of growth temperature on post growth polarisation state 43
5.1 Initial PFM observations . . . 44
5.2 Post growth in-situ annealing . . . 46
5.3 Stoichiometry variation measured by RBS . . . 48
5.4 The microscopic model . . . 48
5.5 Determination of the c-axis distribution in the films . . . 52
5.6 The relationship between polarisation and strain . . . 55
5.7 The contribution of defect dipoles to the polarisation . . . 59
5.8 Dependence on film thickness . . . 60
5.9 Diffractograms for higher temperatures . . . 61
5.10 Conclusion . . . 62

6 Slow Kinetics Intermittent Sputtering 65
6.1 Introduction . . . 65
6.2 Results and discussion . . . 66
6.3 Conclusion . . . 70

7 Non-Ising domain walls in lead titanate thin films 71
7.1 Monodomain samples: written domains . . . 72
7.2 Polydomain samples: intrinsic domains . . . 73

8 Conclusions and perspectives 79

A Growth conditions 83

Remerciements 85

Bibliography 87

CHAPTER 1

Introduction

Ferroelectricity, first discovered in Rochelle salts in 1921 [1], is named in analogy to ferromagnetism, as as the property of materials which present several stable polarisation states in the absence of any electrical field, between which one can switch by the application of an electric field. The ferroelectric polarisation stems from a deformation of the crystal lattice, which means that by symmetry, ferroelectric materials are also pyroelectric and piezoelectric. Indeed, it is often for these properties that they are used in applications [2], as well as for their high dielectric constants. However, it was not until the discovery of ferroelectricity in barium titanate ($BaTiO_3$) in the 1940s that the research and technological development around these materials started to grow exponentially. Indeed, $BaTiO_3$ was the first of a new class of oxide ferroelectrics with a the relatively simple perovskite structure, leading to stability at ambient condition and allowing simple processing and much greater ease of theoretical modelling. One of the most prominent materials of this category, on which this thesis will focus, is lead titanate, $PbTiO_3$.

Continuing the analogy to ferromagnetic materials, since several different polarisation states are possible, it stands to reason that multiple polarisation direction would be present in a single sample: such differently polarised regions are called *domains*. The existence of domains opens up new device possibilities - they can be used to store binary information in their polarisation direction, leading to ferroelectric memories [3]. This, however, requires precise control over the domain state so as to not introduce errors. Other properties of the ferroelectric are strongly affected by the presence of domains, as they will reduce the average polarisation of a macroscopic

sample, suppressing the effective pyro- and piezoelectric coefficients. However, in some configurations, the motion under an applied electric field of the boundaries between the different domains, called *domain walls*, can lead to significantly augmented piezo- and dielectric responses. Interestingly, the dielectric response of the walls can sometimes "overshoot", to the point where their contribution can be seen as a local effective negative capacitance [4].

The domain walls themselves have also spawned an interest as their own object of study. Several properties absent from the bulk phase have been demonstrated to appear at the domain walls, most notably conduction in an otherwise insulating material [5]. This conduction raises hopes for domain wall electronics, or entirely reconfigurable domain wall circuitry. Beyond the interest for applications, the breaking of symmetry occurring at a domain wall allows for some non-trivial internal structure. Although it was long believed that the polarisation should uniaxially decrease to zero at the position of the domain walls, making them so-called Ising structures, it has been shown in the last decade that, in many materials, the walls can host complex rotations of the polarisation in Néel or Bloch structures [6], and that the polarisation vector could even loop onto itself in a highly dimensionally constrained volume to form ferroelectric skyrmions [7, 8].

The fast progress made since the 1990s in oxide deposition techniques has allowed further control of ferroelectric thin films, either by applying strain through the choice of substrate, or by growing artificial heterostructures with various properties. Often, this also affected the domain state of the samples, by modifying the elastic and electrostatic boundary conditions of the films. It is for example well known that the period of domains in supperlattices has a fixed dependence on the thickness of the individual ferroelectric layers. However, systematic control of the intrinsic polarisation state in samples with identical structure and boundary conditions is lacking.

This thesis focuses on ways to fabricate very high quality series of $PbTiO_3$ thin films, where the intrinsic polarisation state, stable at room temperature, can be individually chosen for each sample, while having no difference in sample structure, and almost no difference in sample surface and crystalline quality. This was achieved using two techniques developed during this thesis: the control of the intrinsic polarisation configuration using only the deposition temperature, and Slow Kinetics Intermittent Sputtering, an adaptation of the cheap and scalable radio frequency off-axis magnetron sputtering deposition technique, which allows us to obtain very high quality thin films over a broad range of deposition temperatures.

This thesis is organised as follows. Chapter 2 provides the reader with the necessary background in ferroelectricity and the current research on perovskite oxide ferroelectrics. Chapter 3 develops the relevant parts of the phenomenological Ginzburg-Landau-Devonshire theory of ferroelectricity. A

technical introduction to the various characterisation methods used throughout this thesis is given in Chapter 4. This chapter also reviews off-axis radio frequency magnetron sputtering, the deposition technique that was used for all samples in this thesis. Chapter 5 presents our findings of a growth temperature mediated control of the intrinsically stable polarisation state of $PbTiO_3$ thin films, independently of the electrostatic boundary conditions. A model of the microscopic mechanism behind this control is also developed, in excellent agreement with all our observations. Chapter 6 then presents a simple adaptation of off-axis radio frequency magnetron sputtering, which allows us to obtain very high surface and crystalline quality thin films over a broad range of temperatures. The applicability of this technique to other materials is also demonstrated. Finally, Chapter 7 presents the preliminary results of our ongoing work on one application of these thin films that only differ by their polarisation state: second harmonic generation microscopy, combined with statistical analysis of piezoresponse force microscopy domain images, is used to compare the inner structure of intrinsic versus written domain walls.

CHAPTER 2

Background

2.1 Ferroelectricity

2.1.1 Phenomenology

Ferroic materials are defined by the appearance below a critical temperature of a non volatile order parameter (spontaneous magnetisation, polarisation or strain), reversible under the application of the appropriate conjugate field. In particular, below the Curie temperature T_c, ferroelectric materials develop a non-zero electrical polarisation at zero applied electrical field, the so-called *remanent polarisation*, that can be switched between at least two stable configurations by applying an electrical field.

Ferroelectricity is a subset of more broadly occurring polar behaviour. Of the 32 crystallographic symmetry point groups, 20 exhibit a polarisation when subject to a uniform external stress. This is the *piezoelectric* effect. 10 of those piezoelectric crystal classes are *polar*, i.e. they have a fixed spontaneous polarisation. This polarisation can rarely be observed directly, because it will be screened by free charges either from the surrounding medium or from within the crystal. However, since this polarisation is usually temperature dependent, one can detect the flow of screening charge as the temperature is changed, the *pyroelectric* effect. Finally, if this spontaneous polarisation can be switched between two or more stable states using an electrical field, the material is ferroelectric.

This polarisation switching proceeds hysteretically, as can be seen in Fig. 2.1, where, upon the first application of a positive electrical field, the

whole sample will polarise along the field until saturation, at which point a simple linear dielectric response will be observed, then, when lowering the field back to zero, the sample will keep the remanent polarisation. Upon lowering the field even further, past the *coercive field*, the sample will switch polarisation to align with the field once more, and stay in that negative polarisation state if the field is brought back to zero. The sample can then be switched again towards a positive polarisation state by applying a high enough positive field. The *spontaneous polarisation* is often defined by extrapolating the saturated value to zero field. Note that this is a somewhat empirical definition, and that there are no fundamental symmetry arguments that allow us to differentiate between a non-ferroelectric and a ferroelectric polar material. However, this implies that all ferroelectrics are also pyroelectrics, which are all piezoelectrics. Many of the industrial applications of ferroelectrics make use of these other properties, for example in piezoelectric actuators or pyroelectric motion detectors [2].

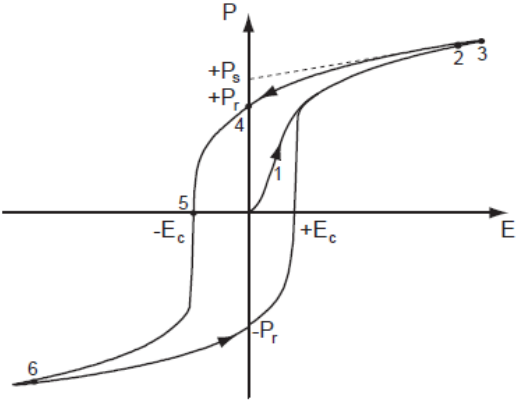

Figure 2.1: A typical ferroelectric switching cycle.

Ferroelectricity was first discovered in Rochelle salt by Valasek in 1921 [1]. However, the research and application really intensified after the discovery of ferroelectricity in $BaTiO_3$ in 1946, both in the USA and in the USSR [9, 10]. $BaTiO_3$ is part of the family of oxides perovskites. They are characterised by their unit formula ABO_3, where A and B are cation with valences ranging from +1 to +3 and +3 to +6 respectively, as well as by their pseudocubic structure, with the A cation at the cube vertices, the B cation at the centre of the cube and the oxygens at the center of the faces, see Fig. 2.2. Depending on the A and B cations, perovskites can have a variety of properties, ranging from insulating to conducting, and displaying different types of structural and magnetic ordering. Ferroelectricity arises, as we will discuss in the following

sections, through a combination of ionic displacements and electronic effects. The simple perovskite structure makes these ferroelectrics ideal for first principle calculations, and their ease of fabrication and excellent properties lead them to a position as the gold standard for applications.

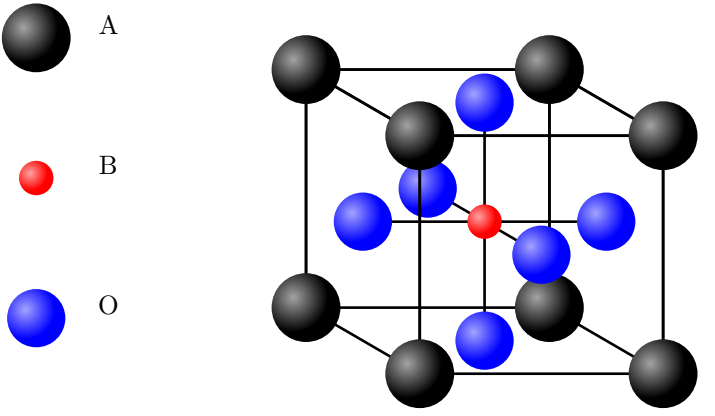

Figure 2.2: Schematic representation of the ABO_3 perovskite unit cell, with the A cations in black, the B cation in red and the oxygens in blue.

2.1.2 Lead titanate, a prototypical oxide ferroelectric

One of the most prominent perovskite ferroelectrics is lead titanate ($PbTiO_3$), extensively characterised via ab-initio and mean-field modelling [11–13]. It is the subject of many experimental investigations, as we will see in the following sections of this chapter, and is one of the end members of the technologically important compounds lead zircontate titanate ($Pb(Zr,Ti)O_3$) and the relaxor ferroelectric lead magnesium niobate-lead titanate (PMN-PT). Both are widely used for their exceptional piezoelectric properties, and prove difficult to replace by lead-free alternatives, for reasons that will become clear in the following sections.

In the high temperature paraelectric phase, $PbTiO_3$ is cubic with a lattice parameter of $a = b = c = 3.969\,\text{Å}$ at the bulk transition temperature $T_c = 760\,\text{K}$. Below T_c, it becomes tetragonal and develops a spontaneous polarisation due to the shift of the titanium atom and of the octahedral oxygen cage. At room temperature, it has the lattice parameters $a = b = 3.904\,\text{Å}$ and $c = 4.152\,\text{Å}$, with the polarisation lying along the c-axis. Since $SrTiO_3$, a readily available substrate, is cubic at room temperature with a lattice parameter of $a = 3.905\,\text{Å}$, very close to the in-plane lattice parameter of $PbTiO_3$, thin films of $PbTiO_3$ epitaxially grown on $SrTiO_3$ will have

their c-axis, and therefore their polarisation, almost exclusively out-of-plane, making for a very simple two state ferroelectric. Despite this apparent simplicity, systems composed of $SrTiO_3$ and $PbTiO_3$ such as multilayers, superlattices or solid solutions continue to reveal surprising properties after close to two decades of intensive research [4, 8, 14–19].

2.1.3 Soft modes

The ferroelectric phase transition can be described as the freezing in of the transverse optical phonon in the centre of the Brillouin zone, as was first done by Cochran [20]. This will happen if the squared frequency of this phonon, which is proportional to the local energy curvature for the corresponding displacements of the atoms, becomes negative in the phonon dispersion calculated for the high symmetry phase: the mode becomes soft. This frequency can be seen as coming from two contributions which balance each other out: the short range repulsive forces between the electron cloud of neighbouring atoms favour the centrosymmetric state and raise the frequency of the transverse optical phonon, whereas the long rang Coulombic dipolar interactions favour the polarised state and lower the frequency of that phonon. When the long range forces overcome the short range ones, the transition occurs.

In $PbTiO_3$, this phonon corresponds to the anti-phase displacements of the Pb and Ti atoms with respect to the oxygen octahedra, see Fig. 2.3 (note that in the figure, the octahedron is shown to be displaced and the Pb atoms fixed). The transition is helped by the fact that the Ti $2p$ orbitals hybridise with the O $2p$ orbitals closest to them, and the Pb $6s$ orbitals hybridise with the O $2p$ orbitals closest to them, which reduces the short range repulsive interactions of the electron clouds [21]. This enhancing effect of lead is why lead based materials continue to dominate the application market. Once the transition is complete, the oxygen atoms, which carry all the negative charge in a simple ionic picture, are displaced with respect to the positive charge of the Pb and Ti ions, creating a dipole moment in each unit cell.

2.1.4 The modern theory of ferroelectricity and Born effective charge

Let us now take a closer look at our intuitive definition of the polarisation in $PbTiO_3$ to understand the problem that needed to be solved by the modern theory of ferroelectricity [22–25]. In addition to these seminal papers, the interested reader is also referred to the very pedagogical introduction by Spaldin [26]. If we look at Fig. 2.3, we can see that, in a single unit cell, the polarisation stems from the displacement of the oxygen octahedron with

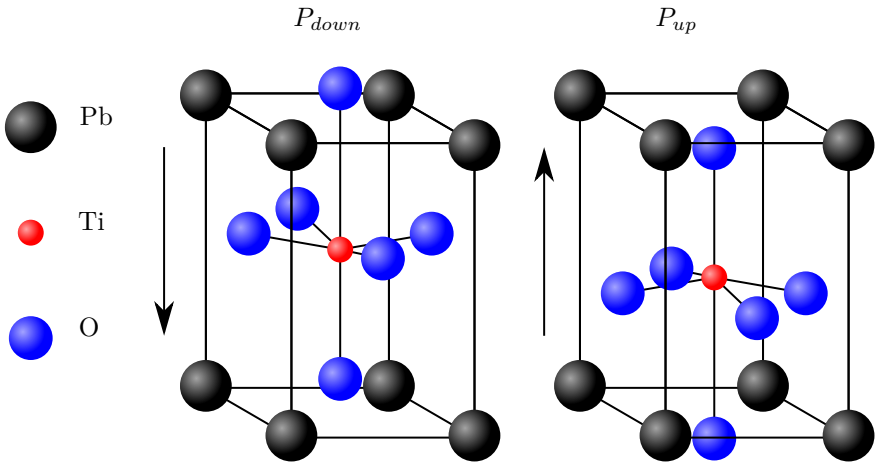

Figure 2.3: Schematic representation of the structural origin of ferroelectricity in $PbTiO_3$. The Ti and O ions displace with respect to the Pb ions, offsetting the centre of positive and negative charge, which creates a dipole moment.

respect to the central titanium atom and the corner lead atoms, leading to a displacement of the centres of negative and positive charge with respect to one another. The polarisation of the unit cell then points from the centre of negative charge to the centre of positive charge.

This naive approach has two problems. First, whereas the positive charge of the heavy atomic nuclei can safely be assumed to be point-like and localised, the valence electrons are in very delocalised Bloch states, such that assigning a charge to an ion is arbitrary. This problem can be tackled by changing basis from the Bloch functions to the localised Wannier function, so that we can assign a point charge to the average position of an electron in a Wannier state, the Wannier centre. One must however keep in mind that the Wannier centre can move differently than the atomic nucleus: indeed, we have seen in the previous section that the cubic to tetragonal transition in $PbTiO_3$ is strongly supported by the hybridisation of Ti $2p$ orbitals and the Pb $6s$ orbitals with the O $2p$ orbitals [21], which implies charge transfer between these orbitals. This is best captured in the Born effective charge of an ion, which is defined as the change in polarisation resulting from a displacement of the corresponding sublattice,

$$Z^*_{ij} = \frac{\Omega}{e}\frac{\delta P_i}{\delta d_j} \tag{2.1}$$

with Ω the unit cell volume, e the electron charge, and d_j the displacement of the sublattice in the direction j. The fact that this charge is substantially larger than the nominal ionic charge in $PbTiO_3$, see Tab. 2.1, is what explains

	Z^*_{Pb}	Z^*_{Ti}	$Z^*_{O_\parallel}$	$Z^*_{O_\perp}$
Nominal	+2	+4	-2	-2
Effective	3.90	7.06	-5.83	-2.56

Table 2.1: Nominal ionic and Born effective charge for the ions in the cubic structure of $PbTiO_3$. $O_\parallel$ refers to movement of the oxygen ion along the axis connecting it to the titanium atom, while $O_\perp$ is perpendicular to that axis. Values from [27].

the large polarisation in that compound.

The second problem may be more important, as in an infinite crystal, the choice of unit cell is not unique. One could therefore, just as validly, choose a unit cell shifted by half our original unit cell, and connect the centre of positive and negative charge in this unit cell, leading to a much greater polarisation in the opposite direction. This is illustrated for a simple one dimensional chain of ions in Fig. 2.4, showing that the polarisation in a crystal is in fact multivalued, since every choice of unit cell can lead to a different value of the polarisation. The saving grace is that, when considering any specific ionic displacement, the change in the polarisation, however it is initially defined, is the same. One therefore uniquely define the change in polarisation going from the centrosymmetric configuration to the distorted one in first principle calculations, while taking care to stay on the same "branch". This is also the quantity that is accessible experimentally, since switching loops such as the one shown in Fig. 2.1 are typically measured by integrating the switching currents, which are a measure of the change in polarisation inside the sample, not of the absolute value of the polarisation itself.

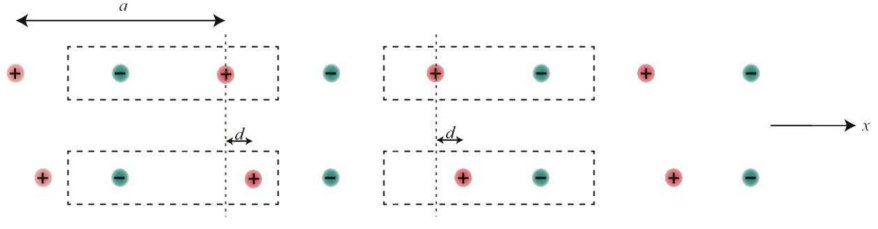

Figure 2.4: The multivalued nature of the polarisation. When a chain of ions is distorted to create a polarisation, the value and the orientation of that polarisation depends on the chosen unit cell. Adapted from [26].

2.2 Domains and domain walls

When a material goes from a paraelectric state to a ferroelectric state, several equivalent new ground states are available, one for each possible polarisation orientation. It is therefore to be expected that the polarisation is not spatially homogeneous. A region of the same polarisation is called a domain, and the separation between domains a domain wall. In the following section, we will discuss the mechanisms that have been used in the past to control the domain configuration, how the properties at domain walls may differ from the properties of the bulk of the sample, and recent observations of new and interesting polarisation textures at domain walls.

2.2.1 The depolarising field

Up to now, we have only considered infinite crystals with uniform polarisation. However, for a finite sample, bound charges will appear at the interface between the ferroelectric crystal and the non-polar surrounding. Theses charges generate a field opposite to the polarisation, which destabilises it: the depolarising field. To maintain the polar state of the sample, these bound charges must therefore be screened by free charges from the surrounding medium. In the case of a capacitor structure, the electrodes contain enough free charges to very efficiently screen the bound charges. For samples exposed to ambient conditions, ions in the air can also serve as screening charges. However, such a screening is never perfect, as the screening charges will not fully overlap with the bound charge, and instead spread over a characteristic screening length λ. This can be modelled by a perfect screener with screening charges positioned a certain effective distance λ_{eff} from the interface. The situation for a capacitor structure in short circuit is represented in Fig. 2.5: there is a voltage drop across the bound charge/free charge double layer, which is in opposite direction on either side of the sample. To keep the short circuit conditions, there must therefore be a voltage drop across the sample thickness equal and opposite to the sum of the voltage drops on each interface. Since this voltage drop is thickness independent, the field across a sample is inversely proportional to its thickness. The depolarising field therefore more strongly affects very thin films, and leads to a shallower energy double well and a narrower ferroelectric switching loop, see Fig. 2.6.

Domain walls are energetically costly. For example, Meyer and Vanderbilt [29] calculated the creation energy of 90° and 180° domain walls in $PbTiO_3$ from first principles, finding 35 mJ/m^2 and 132–169 mJ/m^2 respectively. For a fixed sample geometry, this energy cost will therefore scale as the sample thickness t and the density of domain walls, which scales as the inverse of the domain width w, $F_w \propto \frac{t}{w}$. However, because of the depolarising field, it can be even more costly to maintain a monodomain state over a wide area. Indeed,

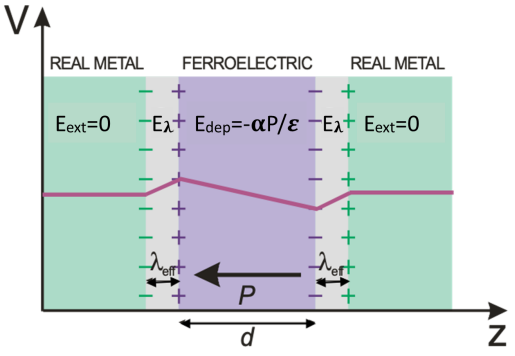

Figure 2.5: The depolarising field from imperfect screening by real electrodes. The bound charge induced by the polarisation P is screened by free charges placed an effective distance λ_{eff} away, leading to a fixed voltage drop over the thickness d of the sample. Figure courtesy of C. Lichtensteiger.

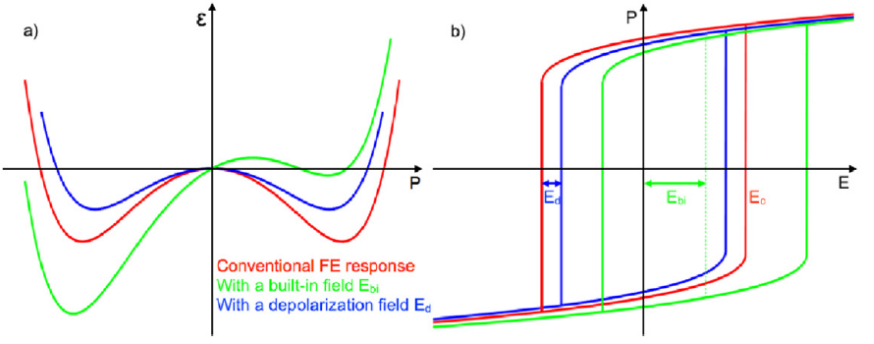

Figure 2.6: Effect of a depolarising field and a built in field on (a) the double well potential and (b) the ferroelectric switching loop. Adapted from [28].

by forming small domains of opposing polarisation, the opposite bound charge from neighbouring domains will effectively compensate, reducing the depolarising field and the associated energy cost. However, the stray fields from the bound charges of the alternating domains will still penetrate over a thickness of the order of the domain width w, $F_d \propto w$. Minimising the total energy $F = F_w + F_d$ with respect to the domain width then yields the famous Kittel law [30], also known as Landau-Lifshitz scaling [31], which states that the domain width is proportional to the square root of the thickness of the sample, $w \propto \sqrt{t}$. Despite its simplicity, this scaling was shown to hold true over 6 decades, and is fully generalisatble to both ferromagnetic and ferroelectric domains [32].

This energy cost of the monodomain state points to an easy way to control the domain state inside a film: by changing the electrostatic boundary conditions, one can change λ_{eff} and therefore the strength of the depolarising field, changing the energy cost of a monodomain state.

A deceptively simple strategy to increase λ_{eff} is to insert dielectric spacer layers between the ferroelectric and its electrodes. This physically puts the screening charges further away from the bound charges at the interface, and therefore adds a length $\lambda' = \frac{t}{\epsilon}$ to the effective screening length, where t is the thickness of the spacer layer and ϵ is its dielectric constant. We explored this idea by comparing several series of samples with and without spacer layers [17]. For 50 nm lead titanate ($PbTiO_3$, PTO) thin films grown epitaxially on strontium titanate ($SrTiO_3$, STO) substrates with a strontium ruthanate ($SrRuO_3$) back-electrode, adding just 2 nm of dielectric STO between the film and the electrode increased the depolarising field enough to go from a monodomain to a polydomain state, see Fig. 2.7. Furthermore, a clear dependence on the spacer layer thickness was shown: for 20 nm PTO films, an STO spacer layer of one unit cell thickness still resulted in a monodomain state, whereas thicker spacers all resulted in a polydomain state. The stability of the switched polarisation in these samples was also analysed, showing that written regions of uniform polarisation would not only switch back much faster in samples with a thicker spacer layers (larger depolarising field), but the way this backswitching occurred was also qualitatively different, with domains appearing inside the written region, whereas, in samples with a thinner spacer layer, written regions "collapsed" from the edges inwards. A similar concept was used by Liu *et al.* [33], where a dielectric STO spacer was inserted between two layers of lead zircontate titanate ($Pb(Zr_{0.2}Ti_{0.8})O_3$), creating a strong depolarising field in both layers. It was shown that this strongly reduced the effective coercive voltage needed to switch the structure, as schematised in Fig. 2.6.

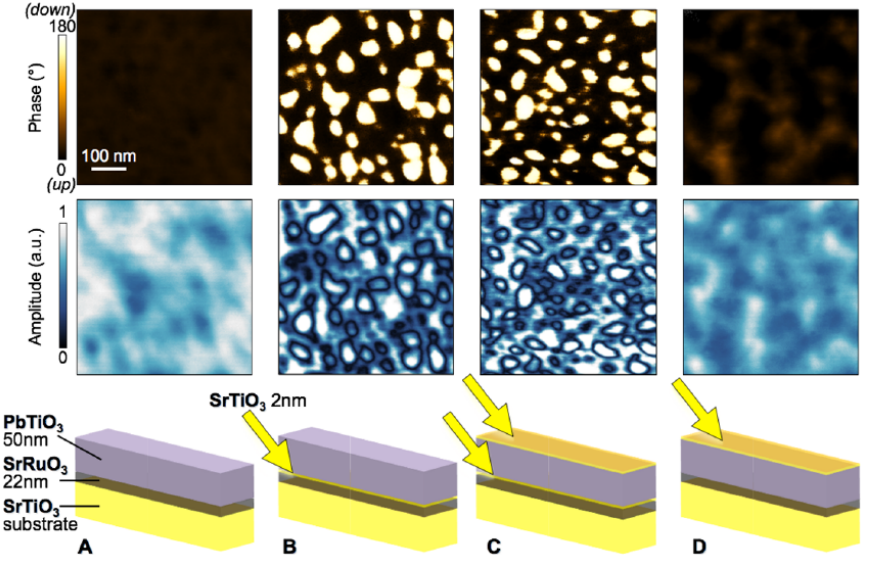

Figure 2.7: Inserting two nanometers of dielectric $SrTiO_3$ between a $PbTiO_3$ layer and its back electrode increases the depolarising field sufficiently to force the sample to break into domains. Adapted from [17].

2.2.2 The built-in field

Another phenomenon which can have a strong effect on the domain configuration of a sample is the appearance of a built-in field. Unlike the depolarising field, which destabilises all polarisation directions equally, the built-in field favours one specific polarisation orientation, lowering its energy and raising the energy of the opposite orientation, see Fig. 2.6. This built-in field can have several origins: the electrostatic boundary conditions can cause it, for example if there is an asymmetry in the screening of negative and positive bound charges, or band bending at the interfaces due to different work functions of the electrode, but it can have internal sources, notably flexoelectricity, where a strain gradient throughout the film acts like an external electrical field [34, 35].

We analysed [28] the built-in field for, among others, the samples used in our previous study [17]. We showed that adding a dielectric spacer layer drastically reduces the built-in field otherwise present in these films, which may also explain why samples without spacer layer are monodomain, while adding the spacer layers produces polydomain films. Furthermore, the built-in field seems to decrease with increasing spacer thickness. Strikingly, the value measured for the built-in field depends on the material of the electrode used to determine it: for SSPFM measurements (see Sect. 4.1.2) the type of metallic tip used had a significant effect on the values measured on the same samples, and area measurements using an oxide electrode grown *in-situ* show an even higher built-in field than samples without spacers or top electrodes.

While this work only demonstrated going from a monodomain state in one direction to a polydomain state, others have achieved complete polarisation reversal using the built-in field. Noh and co-workers [36, 37] showed that for bismuth ferrite thin films grown at various growth temperatures on strontium titanate, both out-of-plane polarisations could be achieved as-grown. The mechanism at work in this case was that depending on the growth temperature, the relaxation state of the film would change. This created a strain gradient, which acts as a built-in field through flexoelectric coupling. This flexoelectric field was larger than the built-in field due to the electrostatic boundary conditions, pushing the sample toward the opposite polarisation direction. The built-in field was then stabilised by defect dipoles. This mechanism is summarised in Fig. 2.8.

Another method to control the electrostatic boundary conditions of a thin film to modify its polarisation direction was explored by Stephenson and co-workers in a series of papers [38–40]. They showed that by subjecting a $PbTiO_3$ film to various partial pressures of oxygen *in situ* after the growth, they could reversibly switch their polarisation. They also showed that the transition temperature was affected by oxygen partial pressure, as can be seen in the phase diagram of Fig. 2.9. Their observations are explained by

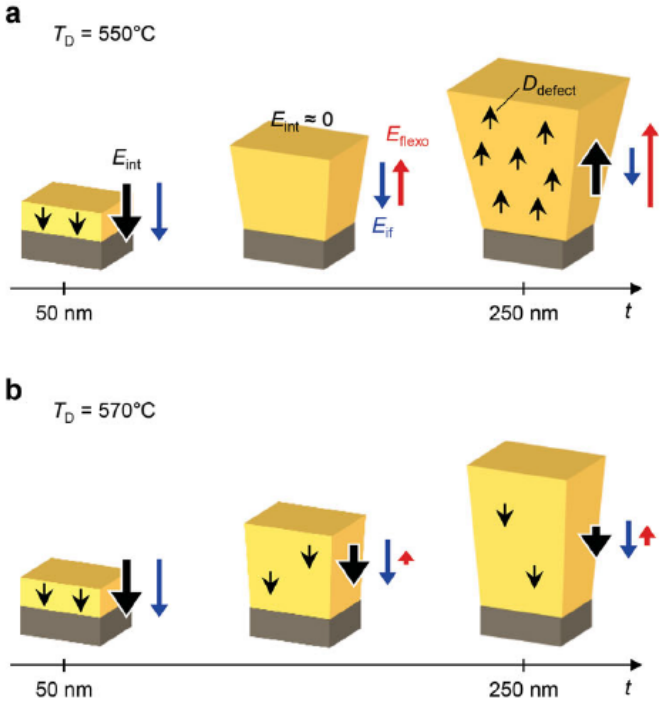

Figure 2.8: Schematic illustration of the control of the built-in field in $BiFeO_3$ thin films (E_{int}, large black arrows) by changing the relaxation state. (a) For a growth temperature of 550 °C, the thin films were very relaxed, leading to a flexoelectric contribution (E_{flexo}, red arrows) to the built-in field that depends on sample thickness, and that is opposed to the built-in field from the interfaces (E_{if}, blue arrows). In the thickest samples, the flexoelectric contribution is bigger than the interface contribution, leading to an overall built-in field in the opposite direction. (b) For a growth temperature of 570 °C, the films did not relax as much, leading to no change in direction of the built-in field with film thickness. Adapted from [37].

the preferential screening of the up polarisation by oxygen ions, whereas the down polarisation is preferentially screened by oxygen vacancies at the surface of the film. In this way, high oxygen partial pressures stabilised an up polarised state, and low oxygen partial pressures stabilised a down polarised state.

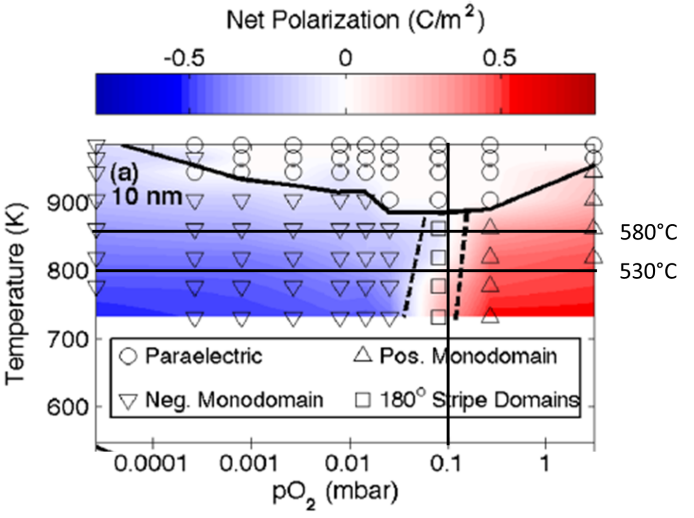

Figure 2.9: Equilibrium polarisation state of a 10 nm film of $PbTiO_3$ with a $SrRuO_3$ bottom electrode, as a function of temperature and oxygen partial pressure, measured *in situ* by Highland *et al.* [40]. For high partial pressures the film is up polarised, whereas it is down polarised for low partial pressures. In the intermediate partial pressure regime, the polarisation orientation depends on the temperature. For comparison, we indicate the temperatures (black horizontal lines) and oxygen partial pressure (black vertical line) we use during growth (see Appendix A), which are very close to this critical region. Adapted from [40].

2.2.3 Conducting domain walls and domain wall nanoelectronics

Domains strongly affect the properties of ferroelectrics. They are responsible for strong changes in the dielectric response, as was first shown by Zhang *et al.* for lead zirconate titanate ceramics [41]. This was subsequently confirmed in several other materials both experimentally [42–44] and theoretically [45, 46]. The mechanism at play is that the expansion of the domains aligned with the external field and the contraction of domains aligned opposite is less energetically costly than changing the polarisation of the

sample macroscopically. This is particularly prevalent in $PbTiO_3/SrTiO_3$ superlatices, where there is a high density of domains [16]. Interestingly, this effect can "overshoot", leading to an effective negative capacitance in a ferroelectric layer sandwiched between dielectrics [47, 48], as was recently demonstrated experimentally by Zubko *et al.* [4].

Maybe more surprisingly, domain walls themselves can present properties that are either very different or entirely absent in the parent material. There have been, for example, reports of polar walls in non-polar materials [49], ferromagnetic walls in antiferromagnetic ferroelectrics [50], and photovaltaic effects localised on the wall [51]. We will focus in this section on the appearance of conduction at domain walls in insulating materials and the possibility that they open for reconfigurable nano-electronics. Conducting domain walls were first reported for oxide ferroelectrics in $BiFeO_3$ [5], where the walls were later shown to be attraction sites for charged defects inside the film [52]. Following this initial report, many other material were found to have conducting domain walls, with a variety of conduction mechanisms proposed to explain it: $Pb(Zr_{0.2}Ti_{0.8})O_3$, where the mechanism is similar to that in $BiFeO_3$ [53], charged domain walls in $BaTiO_3$ [54] and several hexagonal maganites [55], and tilted domain walls in $LiNbO_3$ single crystals [56], where the uncompensated bound charge at the domain wall attracts charge carriers.

Already the first paper by Seidel *et al.* [5] proposed a way to use these conducting domain walls to create multi-level data storage. Others have since expanded on this idea, opening a whole field of possible applications regrouped under the term domain wall nanoelectronics [57, 58]. One example of a possible application would be to use conducting domain walls as reconfigurable nanowires in miniaturised electronics. Several key technological discoveries have been made in this direction, such as the precise injection of a domain wall using micro-fabricated holes in a ferroelectric lamella to focus the electric field [59], or the precise control of domain wall motion through carefully timed voltage pulses [60]. Even more recently, a first ferroelectric domain wall based non-volatile memory was reported, based on the creation and annihilation of conducting domain walls between two electrodes [61].

2.2.4 Non-Ising domain walls and exotic polarisation textures

The high strain-polarisation coupling in ferroelectrics makes it very costly for the polarisation to not point along a fixed crystallographic direction. The fact that the polarisation stems from a presumably continuous deformation of the unit cell also gives it a natural way to reduce when it approaches a domain wall, unlike the magnetisation in ferromagnets which stems from a quantised spin. It is therefore reasonable to assume that all 180° domain walls

in ferroelectrics would be of Ising type (see Fig. 2.10), where the polarisation goes to zero at the wall. Recent theoretical and experimental works have challenged this notion, and we will look in this section at some examples of non-Ising polarisation textures that have been reported.

Several theoretical studies over the last decade [6, 62–67] have analysed the domain walls of uniaxial oxide ferroelectrics such as $BaTiO_3$, $LiNbO_3$, and $PbTiO_3$, and predicted them to have non-Ising components, namely to have a non-zero component of polarisation at the wall, either perpendicular to the wall (Néel-type) or in the plane of the wall (Bloch-type), see Fig. 2.10. The latter is a chiral structure, because it cannot be mapped onto its mirror image using only rotations and translations. Experimental confirmation came when De Luca *at al.* [68] demonstrated a Néel-type component of polarisation inside written walls in $Pb(Zr_{0.2}Ti_{0.8})O_3$ using scanning transmission electron microscopy and second harmonic generation. This was confirmed by Cherifi-Hertel *et al.* [69], who also found a Bloch-type component in written walls in single crystal $LiTaO_3$ using second harmonic generation.

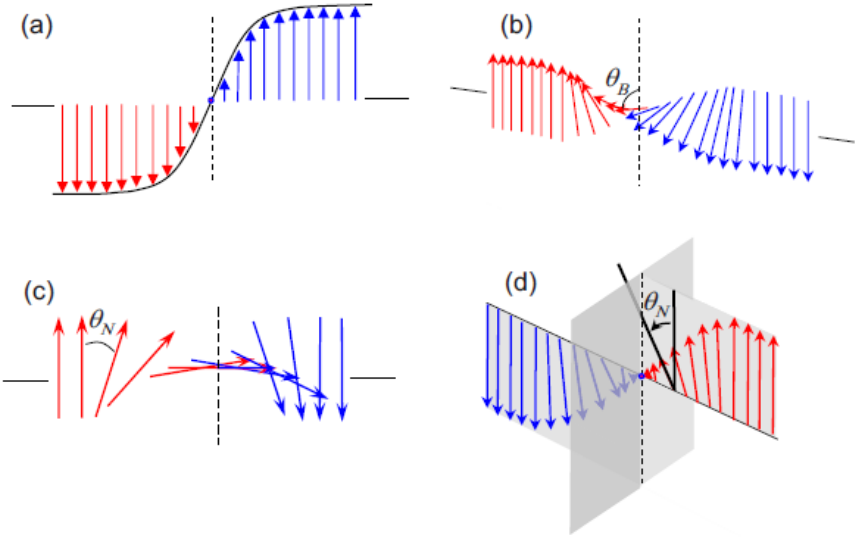

Figure 2.10: The different types of 180° domain walls. (a) The Ising type wall, with no rotation of the polarisation. (b) The Bloch type wall, where the rotation is in the plane of the wall. (c) The Néel type wall, where the rotation is in a plane perpendicular to the wall. (d) A combined Néel-Ising type wall, which shows both reduction and rotation of the polarisation. Adapted from [6].

Many more complex and exotic polarisation textures have since been reported. Yadav *et al.* [19] showed ordered arrays of polar vortices inside

the ferroelectric layers of $PbTiO_3/SrTiO_3$ superlattices grown on $DyScO_3$ directly by high resolution transmission electron microscopy. A "supercrystal" of very ordered flux closure domains was stabilised in the same system by the same group [70] using ultrafast light pulses. A similar, although spontaneously ordered phase was observed by Hadjimichael *et al.* [71] in $PbTiO_3/SrRuO_3$ superlattices grown on $DyScO_3$. Most recently, ferroelectric skyrmions were predicted in $PbTiO_3$ [7] and subsequently measured [8] in $PbTiO_3/SrTiO_3$ superlattices grown on $SrTiO_3$ substrates.

CHAPTER 3

Ginzburg-Landau-Devonshire approach to ferroelectrics

In this chapter, we will discuss the theory of phase transitions developed by Landau [72, 73], subsequently extended with Ginzburg to include non-homogeneous systems [74], and adapted for ferroelectrics by Devonshire [75–77].

3.1 Conjugate variables

In thermodynamics, it is assumed that we can describe the free energy contained in a dielectric in terms of three variables, chosen in the pairs temperature T and entropy S, stress σ and strain e, and polarisation P and electrical field E. For each of the eight choices for *independent variables*, there exists a corresponding *thermodynamic potential* that can be used to predict the state of the system if those variables are fixed. Indeed, in an experimental set up where, for example, temperature, stress, and polarisation are fixed, the dependent variables, here entropy, strain and electrical field, will spontaneously assume a value such that the corresponding thermodynamic potential, in this case the Helmoltz free energy, is minimised. To go from one thermodynamic potential to another, one uses the Legendre transformation, which in physical terms corresponds to adding a term that takes the energy cost of the new applied field into account. For example, to go from a potential with fixed polarisation to a potential with fixed electrical field, one needs to add the term $-EP$, since this is the energy cost for the material in an applied electrical field.

To be able to predict the response of our sample, the idea of the phenomenological Landau-Devonshire approach is to Taylor expand the relevant thermodynamic potential close to a reference phase, and to fit the coefficients of this expansion to experiments. This strategy however quickly breaks down on its own, since the number of coupling parameters becomes untractable. Indeed, while temperature and entropy are scalars, meaning their coupling coefficient is a scalar, P and E are vectors, so that their coupling coefficient is a first rank tensor, and e and σ are first rank tensors, making their coupling coefficient a second rank tensor. Overall, even if Maxwell relations limit the amount of independent elements, a complete coupling matrix would have 55 independent elements, too many to reasonably fit. One must therefore make some assumptions based on a physical understanding of the system.

3.2 Symmetry and physical arguments

The first assumption is going to be that the same expansion can describe both the high temperature non polar phase as well as the low temperature polar phase. This places heavy constraints on the coupling coefficients between the different variables, since they are material properties and therefore must not change under a symmetry operation that does not change the material. Only cases where the non polar phase is centrosymmetric are considered, which forces all odd-rank tensor coefficients to be 0. Furthermore, one assumes that the strain with respect to the reference phase is sufficiently small that high order strain terms can be ignored.

This drastically reduces the number of terms that we have to consider. First, the expansion in terms of the polarisation

$$a_i P_i^2 + a_{ij} P_i^2 P_j^2 + a_{ijk} P_i^2 P_j^2 P_k^2 + ... \tag{3.1}$$

is usually truncated either at order four or at order six, to avoid instability towards infinite polarisation. Next, the energy due to the strain state is

$$\frac{c_{ijkl}}{2} e_{ij} e_{kl} \tag{3.2}$$

It is analogous to the potential energy stored in a spring. c_{ijkl} is the stiffness tensor. The coupling between strain and polarisation is called electrostriction and is given by:

$$- q_{ijkl} e_{ij} P_k P_l \tag{3.3}$$

where q_{ijkl} is the corresponding electrostriction tensor. Finally,

$$- P_i E_i - e_{ij} \sigma_{ij} \tag{3.4}$$

is the energy associated with the externally applied electric field and stress.

In principle, all these coupling terms are temperature dependent. However, the final assumption is that the leading temperature dependence is carried by the first term in the polarisation expansion, and that it can be restricted to a linear dependence around the Curie temperature, $a_{ij} = \beta_{ij}(T - T_c)$, with $\beta > 0$.

We are now equipped to derive some classical results for ferroelectrics. Let us start in the simplest possible configuration: a uniaxial ferroelectric in the absence of any strain or stress. We will also assume that we can truncate the expansion in terms of polarisation at order four. To simplify the notation, let $a_{11} = \alpha/2$, and $a_{1111} = \gamma/4$. The Gibbs free energy is then given by

$$G = \frac{\alpha}{2}P^2 + \frac{\gamma}{4}P^4 - EP \tag{3.5}$$

Note that for the system to be stable against $P \to \infty$ we must have $\gamma > 0$. Under fixed electrical field, the polarisation of the system will evolve to minimize this free energy. One therefore gets the equation

$$0 = \alpha P + \gamma P^3 - E \tag{3.6}$$

Let us first consider the case of no applied field, $E = 0$, to find the spontaneous polarisation of the system. For $\alpha \geq 0$ the only solution is $P_s = 0$. For $\alpha < 0$, the non-trivial solution is

$$P_s^2 = -\frac{\alpha}{\gamma} = \frac{\beta}{\gamma}(T_c - T) \tag{3.7}$$

where the temperature dependence of the α coefficient was reintroduced in the last equality. We see that we have a second order phase transition, where the order parameter P_s appears smoothly below $T = T_c$. Below $T = T_c$, $G(P)$ takes the well known shape of a double-well potential, such as can be seen in Fig. 2.6. To describe a first order phase transition, we need to let $\gamma < 0$, and therefore reintroduce the sixth order term of the expansion on terms of polarisation for stability reasons. The interested reader is referred to any classical text on ferroelectrics for details, for example Ref. [2].

One can now compute the dielectric stiffness or reciprocal permittivity $\kappa = \frac{1}{\chi} = \frac{\partial E}{\partial P}$. Eq. 3.6 is solved for E, then a derivation is performed to find

$$\kappa = \alpha + 3\gamma P_s^2 \tag{3.8}$$

This leads to classical Curie-Weiss behaviour, where $\kappa = \beta(T - T_c)$ for $T > T_c$ and $\kappa = 2\beta(T_c - T)$ for $T < T_c$.

3.3 Dealing with inhomogeneity: the Ginzburg-Landau theory

Up to this point, we have only considered the case of homogeneous strain and polarisation throughout the material. Let us now examine what modifications are necessary for the theory to be able to tackle cases where these quantities vary inside the sample.

First, one must now consider an energy density that explicitly depends on position, whereas the total energy will be obtained by integrating the density over the volume. This can be easily done by making the following substitutions in the previous expansion:

$$\begin{aligned} G &\to \Phi_G(x) & P_i &\to P_i(x) \\ e_{ij} &\to e_{ij}(x) & G &= \int \Phi_G(x) dV \end{aligned} \tag{3.9}$$

However, to not needlessly burden the notation, the dependence on position will not be explicitly stated in the following.

One also has to consider the energy cost of having close neighbours not be in the same polarisation state. To take this into account, the lowest order symmetry-allowed term is of the form

$$\frac{g_{ijkl}}{2} \frac{\partial P_i}{\partial x_j} \frac{\partial P_k}{\partial x_l} \tag{3.10}$$

where g_{ijkl} is called the correlation energy tensor.

There are two more terms allowed by symmetry, and of first order both in strain and in the derivatives of the strain

$$-\frac{f_{ijkl}}{2} \left[P_k \frac{\partial e_{ij}}{\partial x_l} - e_{ij} \frac{\partial P_k}{\partial x_l} \right] \tag{3.11}$$

These terms link a strain gradient with the polarisation, and are needed to describe the flexoelectric effect (see, for example, [34]), as we shall see subsequently. f_{ijkl} is therefore called the flexocoupling tensor.

Taking all the terms we have mentioned in this chapter together, one can write the expansion of the Gibbs free energy density as

$$\begin{aligned} \Phi_G =& a_i P_i^2 + a_{ij} P_i^2 P_j^2 + a_{ijk} P_i^2 P_j^2 P_k^2 \\ &+ \frac{c_{ijkl}}{2} e_{ij} e_{kl} - q_{ijkl} e_{ij} P_k P_l \\ &+ \frac{g_{ijkl}}{2} \frac{\partial P_i}{\partial x_j} \frac{\partial P_k}{\partial x_l} - \frac{f_{ijkl}}{2} \left[P_k \frac{\partial e_{ij}}{\partial x_l} - e_{ij} \frac{\partial P_k}{\partial x_l} \right] \\ &- P_i E_i - e_{ij} \sigma_{ij} \end{aligned} \tag{3.12}$$

where P is the polarisation, e is the strain, c is the stiffness tensor, q is the electrostriction tensor, g is the correlation energy tensor, and f is the flexocoupling tensor.

One final adjustment which has to be made is that to minimise $G = \int \Phi_G dV$, partial derivatives can no longer be used in a straightforward manner (as was done in Eq. 3.6 for example). Fortunately, one can resort to the Euler-Lagrange equation

$$\frac{\partial \Phi_G}{\partial A} - \frac{d}{dx}\left(\frac{\partial \Phi_G}{\partial(\partial A/\partial x)}\right) = 0 \tag{3.13}$$

where A stands for P and e, to find the function $A(x)$ that will minimize G, using appropriate boundary conditions.

As an example, let us consider the case $A = e_{ij}$. For simplicity, we neglect the electrostriction term. We therefore have

$$\frac{\partial \Phi_G}{\partial e_{ij}} = c_{ijkl}e_{kl} + \frac{f_{ijkl}}{2}\frac{\partial P_k}{\partial x_l} - \sigma_{ij} \tag{3.14}$$

$$-\frac{d}{dx}\left(\frac{\partial \Phi_G}{\partial(\partial e_{ij}/\partial x)}\right) = \frac{f_{ijkl}}{2}\frac{\partial P_k}{\partial x_l} \tag{3.15}$$

which leads us to the following expression for the mechanical stress

$$\sigma_{ij} = c_{ijkl}e_{kl} + f_{ijkl}\frac{\partial P_k}{\partial x_l} \tag{3.16}$$

where the effect of the converse flexoelectric effect is apparent: a gradient in polarisation leads to a stress inside the material.

3.4 Applying the constraints of thin film geometry

We can significantly simplify the expression for the Gibbs free energy density (Eq. 3.12) by implementing the constraints linked to our sample geometry, and by limiting our analysis to monodomain samples. First, we assume our samples to be homogeneous in-plane. All quantities are therefore assumed to vary only out-of-plane, and we define $x_3 \equiv z$. Our films are uniaxialy polarised out-of-plane, therefore $P_1 = P_2 = 0$ and $P_3 = P(z)$. Furthermore, the reciprocal space maps of our samples (see, for example, Fig. 5.2) show no relaxation, implying that the in-plane strain is constant and given by the mismatch strain with the substrate, u_m. The substrate is cubic $SrTiO_3$, so we have, in Voigt notation, $e_1 = e_2 = u_m$ and $e_6 = 0$. The upper surface of the film is free, therefore $\sigma_3 = \sigma_4 = \sigma_5 = 0$. We also let $\sigma_1 = \sigma_2 = \sigma$ and

$e_3 = e_3(z)$. Putting all of this together we get

$$\begin{aligned}\Phi_G =& a_3P^2 + a_{33}P^4 + a_{333}P^6 \\ &+\frac{1}{2}c_{11}(2u_m^2 + e_3^2) + c_{12}(u_m^2 + 2u_m e_3) - q_{11}e_3P^2 - 2q_{12}u_m P^2 \\ &+\frac{g_{1111}}{2}\left(\frac{\partial P}{\partial z}\right)^2 - \frac{f_{11}}{2}\left(P\frac{\partial e_3}{\partial z} - e_3\frac{\partial P}{\partial z}\right) \\ &-PE - 2\sigma u_m\end{aligned} \tag{3.17}$$

where we have dropped the explicit z dependence of P and e_3 to simplify the notation. The Gibbs free energy per unit area is then obtained by integrating over the thickness of the sample

$$\frac{G}{S} = \int \Phi_G dz \tag{3.18}$$

We can now predict properties by minimising G using Euler's equation, Eq. 3.13. The values used throughout this thesis are given for the relevant coefficients in Tab. 3.1.

Symbol	Value	Units	Reference
a_3	$3.8 \times 10^5(T - 752)$	JmC^{-2}	[15]
a_{33}	4.229×10^8	Jm^5C^{-4}	
a_{333}	2.6×10^8	Jm^9C^{-6}	
c_{11}	1.746×10^{11}	Jm^{-3}	
c_{12}	0.794×10^{11}		
q_{11}	1.14×10^{10}	JmC^{-2}	
q_{12}	4.63×10^8		
f_{11}	-17	JC^{-1}	[35]

Table 3.1: The expansion coefficients used throughout this thesis.

CHAPTER 4

Experimental methods

In this chapter, we aim to provide enough information on the experimental techniques used during this work for the reader to appreciate the reach and limitations of the experimental results presented in the following chapters. We also include a list of useful references to the reader interested in learning more on a specific technique.

4.1 Scanning probe microscopy

Scanning probe microscopy refers to a set of microscopy techniques where a physical probe is brought close to a sample surface. An image is then formed by recording a physical interaction between the probe and the sample at discrete points while scanning one with respect to the other. The first scanning probe microscope was the scanning tunnelling microscope developed by Binning and Rohrer [78] in 1981. In this section we will go into more details about atomic force microscopy (AFM) and piezoresponse force microscopy (PFM), two techniques that use a similar setup, but probe different physical properties.

4.1.1 Atomic force microscopy

AFM produces an image of the topography of a surface with Å vertical resolution and nm horizontal resolution. The probe used is a sharp tip (equivalent radius of the order of 20 nm) nanofabricated at the end of a

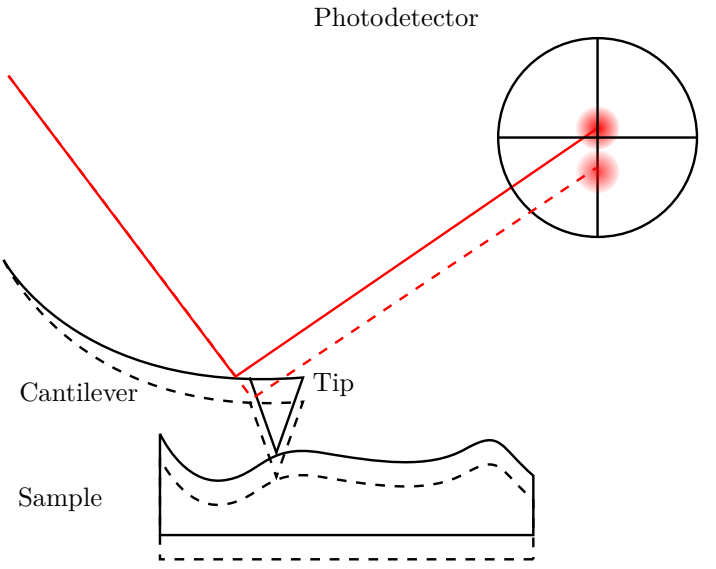

Figure 4.1: Working principle of the optical beam deflection detection scheme: the bending of the cantilever is translated to a shift of intensity between the top part and the bottom part of the four quadrant photodetector.

reflective cantilever. This tip is brought in close contact with the sample, and the tip and the sample are then scanned with respect to each other using a pizoelectric tube scanner. Whether the tube moves the tip or the sample depends on each particular design. A feedback loop is used to keep the distance between the tip and the sample constant, so that the vertical displacement needed to achieve this results in an image of the surface of the sample.

There are two main mechanisms used to determine the distance between the tip and the sample (the input to the feedback loop), resulting in two main topographic "modes". In contact mode, the tip is brought in hard contact with the surface, and the distance is monitored by observing the deflection of the cantilever. To this end, a laser is commonly reflected from the cantilever onto a four quadrant photodetector. Deflecting the cantilever upwards will result in more intensity on the upper quadrants of the detector, and less intensity on the lower quadrants. This detection scheme, sketched in Fig. 4.1, is called optical beam deflection, and is a very indirect measure of the actual displacement of the tip: it measures a deflection angle, which is linked through the spring constant of the cantilever to the force applied to the tip, which in the end indicates the height of the sample. However, it is sufficient to feed back on. To maintain a constant deflection, the surface of the sample must always be precisely at the same height with respect to the

tip, and it can therefore be used to map out the topography of the sample. Tapping mode, on the other hand, consists of oscillating the cantilever at its resonance frequency, then filtering out the response on the photodetector at that specific frequency using a lock-in amplifier. This allows us to observe the amplitude and phase of the response as the tip is brought close to the surface. For a given excitation amplitude, the amplitude of the response will go down when the tip starts touching the sample. The feedback loop then changes the distance between the tip and the sample in such a way as to keep the amplitude of the oscillation constant during scanning. This method exerts less force on the sample and can lead to sharper images, since the feedback signal is more sensitive. However, it is sometimes preferable to be in hard contact with the sample, for example when dust particles have accumulated on the surface of a dirty sample: tapping mode will only measure the particles, whereas contact mode can push them out of the way and reveal the surface underneath, as can be seen in Fig. 4.2.

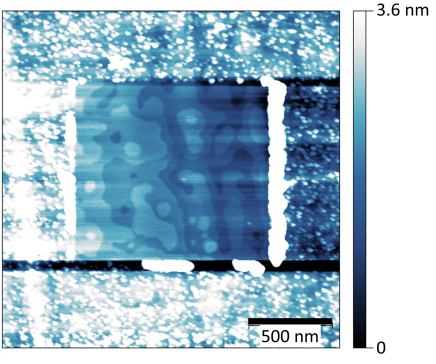

Figure 4.2: AFM topography recorded in tapping mode after a smaller region in the middle was scanned in contact mode. We can see that some of the dust particles obscuring the tapping mode image have been moved out of the central region by the tip during contact mode scanning, revealing the unit cell high steps underneath.

4.1.2 Piezoresponse force microscopy

In PFM, first introduced by Gruverman *et al.*[79], an AFM tip with a metallic coating is used to apply a voltage across a piezoelectric sample. The resulting deformation is then recorded by the deflection of the tip. This signal is typically way below the noise level for a continuous signal acquisition, but it can be detected by exciting the sample at a high frequency (10 kHz to 1000 kHz), and using a lock-in amplifier to consider the response only at that frequency. The signal is then typically demodulated into the amplitude of

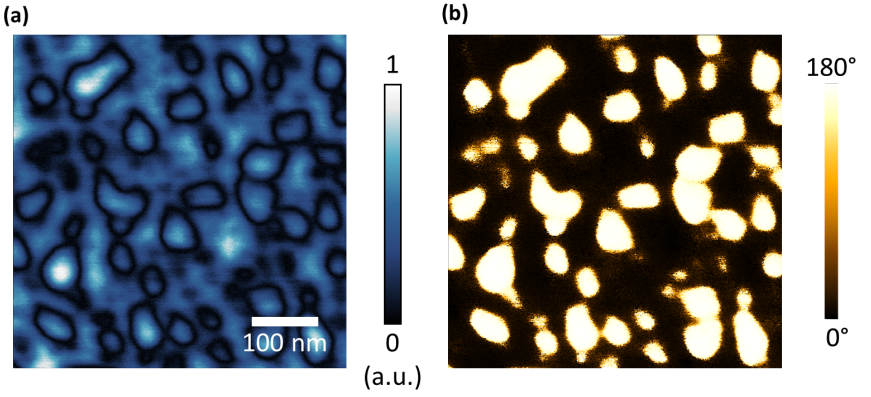

Figure 4.3: A typical PFM (a) amplitude and (b) phase image of a ferroelectric sample with out-of-plane domains. The domains show a 180° phase shift with respect to the background, and the domain boundaries show a sharp amplitude drop.

the response and the phase of the response with respect to the input signal.

The contrast in PFM comes about when ferroelectric materials are measured. Indeed, as seen in Sect. 2.1.1, all ferroelectrics are also piezoelectrics. By symmetry, when the applied voltage causes a certain domain to expand, the same voltage will cause a domain with the opposite polarisation to contract. This leads to a 180° phase shift between the responses of oppositely polarised domains. For out-of-plane polarised domains, this effect is easy to detect in the vertical deflection of the tip, but it can also be used for in-plane domains by analysing the horizontal deflection. Domain walls between 180° out-of-plane domains, on the other hand, do not carry an out-of-plane polarisation, and are therefore not expected to produce a response. Furthermore, the out of phase oscillation will cancel out at the boundary between the domains, causing a sharp drop of amplitude at the domain wall. A typical example of amplitude and phase images for a sample with out-of-plane domains can be seen in Fig. 4.3. The domains show a 180° phase shift with respect to the background, and the domain boundaries show a sharp amplitude drop. The convolution of the imaged feature with the tip shape, a problem common for all scanning probe microscopy techniques, spreads this drop over several nanometers, although it is known from theory and from transmission electron microscopy measurements that the domain wall is an order of magnitude thinner than that. In principle, variations in the PFM amplitude could be connected to local variations of the piezoelectric coefficient, and therefore the local polarisation in ferroelectrics. However, the amplitude image carries many artefacts, caused by, for example, variations in topography and electrostatic interactions between the tip and the sample,

making analysis of this kind at best qualitative.

Dual frequency resonant tracking

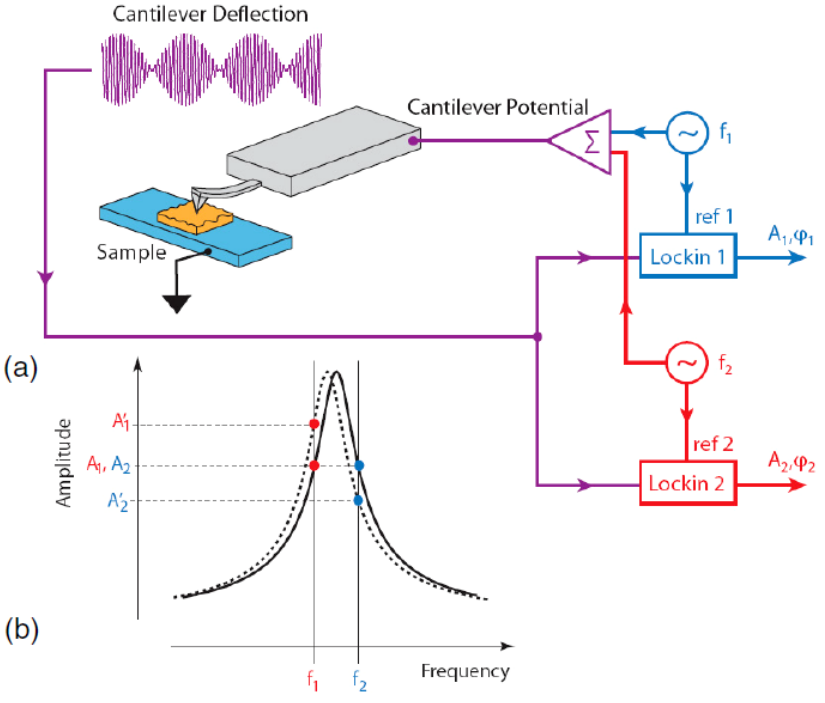

Figure 4.4: The working principle of the DART approach to resonant tracking. (a) Two lock-ins are used to apply two frequencies to the sample, one on either side of the resonance peak. (b) When the resonance peak shifts to lower frequencies, the first amplitude goes up while the second one goes down, and vice-versa when the resonance peak shifts up. By feeding back on the difference between the amplitudes, resonance tracking is achieved. Adapted from [80].

Traditional, "single frequency" PFM is usually done far away (in frequency) from the contact resonance peak, that is the frequency where the cantilever-tip-sample system enters in resonance while keeping the tip and the sample in contact. It can be tempting to take advantage of the increased response close to that frequency to increase the signal to noise ratio, however the resonance can shift significantly while scanning, due to variations in the tip-sample contact. This can lead to strong contrast in amplitude, and even phase flips, without any change of the underlying domain structure. A simple phase-locked loop to track the resonance will fail due to the phase

reversals caused by the domains. Another way of tracking the resonance frequency is therefore needed to be able to take advantage of the increased signal to noise ratio without introducing strong artefacts.

In dual frequency resonance tracking, commercially sold by *Asylum Research* under the name of dual AC resonance tracking (DART)[80], the sample is excited at two frequencies and two lock-in amplifiers are used to demodulate the response signal. One of the frequencies is chosen to be just below the resonance frequency, and the other one just above. In this way, if the resonant frequency shifts down, the amplitude of the response at the first frequency will increase, while the other one will decrease, and vice-versa if the resonant frequency increases. By using a feedback loop to adjust the driving frequencies such that the difference in amplitude remains at zero, while maintaining the difference in frequencies, one can reliably track the resonance peak. This procedure is summarised in Fig. 4.4.

Switching spectroscopy PFM

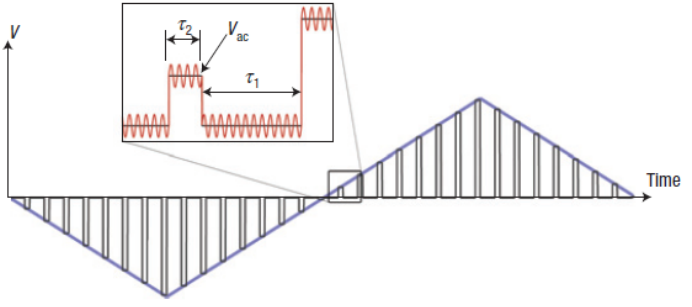

Figure 4.5: The waveform used in SSPFM: voltage pulses of varying intensity are applied for a time τ_2 with a time τ_1 between the pulses. The envelope of the pulses forms a triangular signal. The AC probing voltage is always added on top of the DC voltage pulses. Adapted from [81]

Switching spectroscopy PFM (SSPFM)[82] aims to extract polarisation switching information, such as the coercive voltage and the asymmetry of switching, on a local scale. The technique works by applying a special waveform (a triangular pulse modulated by a sawtooth pattern, see Fig. 4.5) as a DC bias to the PFM tip, on top of the voltage used to read the polarisation. The DC bias ramps up and down in steps, and always returns to zero between steps. This allows us to construct two "loops": the "on" loop consists of the amplitude and phase values measured at each DC voltage while the voltage is applied, while the "off" loop plots the same values measured at zero DC bias, as a function of the bias that was applied just

before in the SSPFM waveform. The off loop therefore allows us to probe the remanent changes induced under the tip by the DC bias, while limiting the electrostatic interaction between the tip and the sample.

Traditionally, the switching properties of a sample are measured using macroscopic electrodes, and the polar state is inferred by integrating switching currents. This method suffers from two main drawbacks, which are in principle avoided by SSPFM. First, the local information, for example on the scale of a single nanodomain or individual nucleation event, is lost by the use of macroscopic electrodes, whereas SSPFM is a local probe. Second, since the polarisation state is determined by the integration of switching currents, any leakage currents will obscure the results, necessitating multiple pass techniques such as PUND, which may still fail to extract a result if the leakage is too important. In SSPFM, the polarisation state is determined by PFM, and is therefore much less sensitive to leakage. However, the drawback is that, while we can be reasonably sure of the voltage applied to a sample trough a macroscopic electrode, in SSPFM the voltage is applied to a complex system consisting of the cantilever, the tip, the interface between the tip and the sample, and finally the sample that is to be measured. SSPFM measurements can therefore be strongly influenced by tip type, tip wear, variations in tip-sample contact, and similar extrinsic factors which are hard to control. To try and minimise the influence of such factors in our results, we only used SSPFM statistically, by collecting a large amount (order 10^2) of loops over a $5 \times 5\mu m^2$ area on each sample, using tips of the same type and of similar wear, and averaging the properties of all loops for each sample.

4.2 X-ray diffraction

X-ray diffraction is a powerful way to probe the crystalline structure of solids. In the case of thin film growth, it allows us to determine the lattice parameters of our film as well as check their epitaxy and crystalline quality. A standard four circle diffractometer such as the *Panalytical* MRD 4 used in this study is schematically represented in Fig. 4.6. The radiation used is the Cu$K\alpha_1$ monochromated to a wavelength of λ =1.5406 Å. ω, χ, and ϕ rotate the sample around the x, y, and z axes, respectively, fixing the direction of the incoming radiation. 2θ is the angle between the incoming and the outgoing radiation.

In a perfect crystal, the x-rays will be diffracted according to Laue's criterion $\boldsymbol{G} = \boldsymbol{q}$, where $\boldsymbol{G} = h\boldsymbol{a}_1^* + k\boldsymbol{a}_2^* + h\boldsymbol{a}_3^*$ is a vector of the reciprocal lattice (h, k, l are integers and $\boldsymbol{a}_i^*$ are the basis vectors of the reciprocal lattice), and $\boldsymbol{q} = \boldsymbol{k} - \boldsymbol{k'}$ is the momentum transferred by the lattice, with $\boldsymbol{k}$ the incoming wave vector and $\boldsymbol{k'}$ the diffracted wave vector. It can be shown that this criterion is equivalent to the Bragg condition for diffraction

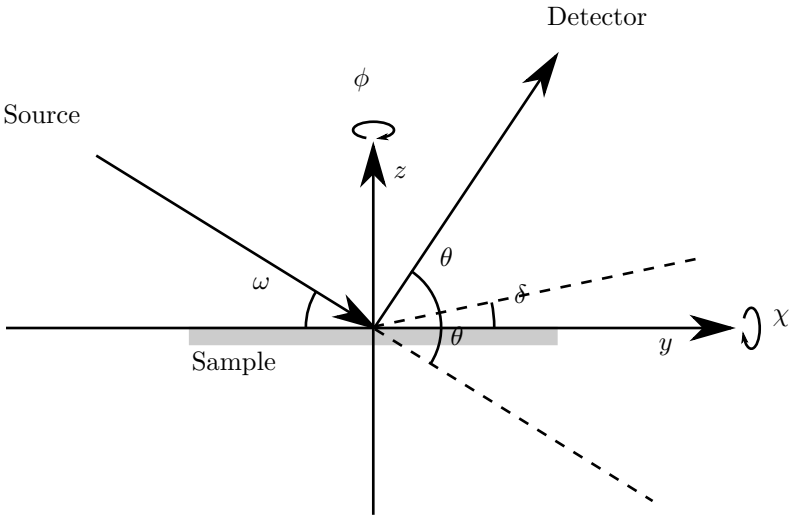

Figure 4.6: Side view of a four circle diffractometer. ϕ and χ are used to orient the sample such that the planes of interest are normal to the diffraction plane formed by the incoming and outgoing beams. ω and 2θ are then used scan different orders of diffraction for this family of planes, by keeping $\delta = \theta - \omega$ constant.

$\lambda = 2d_{hkl} \sin\theta$, where λ is the wavelength of the x-rays, d_{hkl} is the distance between the planes of the lattice with Miller indices (h, k, l), and θ is half the angle between the incoming and the diffracted beams. This gives us a visual interpretation of the different angles available in our diffractometer, and how the different scans will probe the reciprocal space. Probing the reciprocal space will also let us draw conclusions about the real space characteristics of the crystal, in particular the lattice spacing and the epitaxy of our thin films.

In elastic scattering, we have that $|\boldsymbol{k}| = |\boldsymbol{k'}|$. We will now use this fact to construct what is called the Ewald sphere as can be seen in Fig. 4.7. First draw the incoming wave vector such that it originates at a point A in reciprocal space and terminates at the origin O. Then draw a sphere around point A that contains the origin: it is the collection of all possibilities for the vector $\boldsymbol{q} = \boldsymbol{k} - \boldsymbol{k'}$. If a lattice point, corresponding to a lattice vector $\boldsymbol{G}$ is on that sphere, Laue's criterion is fulfilled, and we will detect diffracted x-rays if we set the detector such that $\boldsymbol{k'}$ originates at A and terminates on that lattice point. We can now describe the angles available in the diffractometer in reciprocal space: ω, ϕ, and χ position the sample with respect to the incoming x-ray beam in real space, which corresponds to moving the point A in reciprocal space, and therefore changing the direction of the vector $\boldsymbol{q}$ without changing its length. 2θ on the other hand is the angle between the

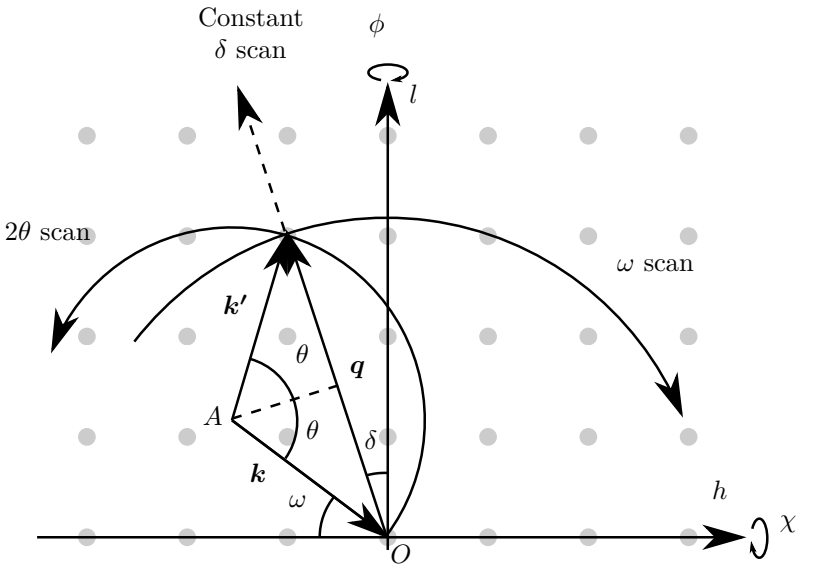

Figure 4.7: A cut through the Ewald sphere for a diffraction at $k = 0$. The effects of scanning the different angles in the diffractometer individually are shown, as well as a simultaneous scan of 2θ and ω, while keeping δ constant.

incoming and outgoing rays, and changing it will move $\boldsymbol{q}$ on the Ewald sphere, changing both its length and its orientation. However, by simultaneously scanning both θ and ω by the same amount, only $|\boldsymbol{q}|$ will change, and we can probe any straight line passing through the origin of reciprocal space.

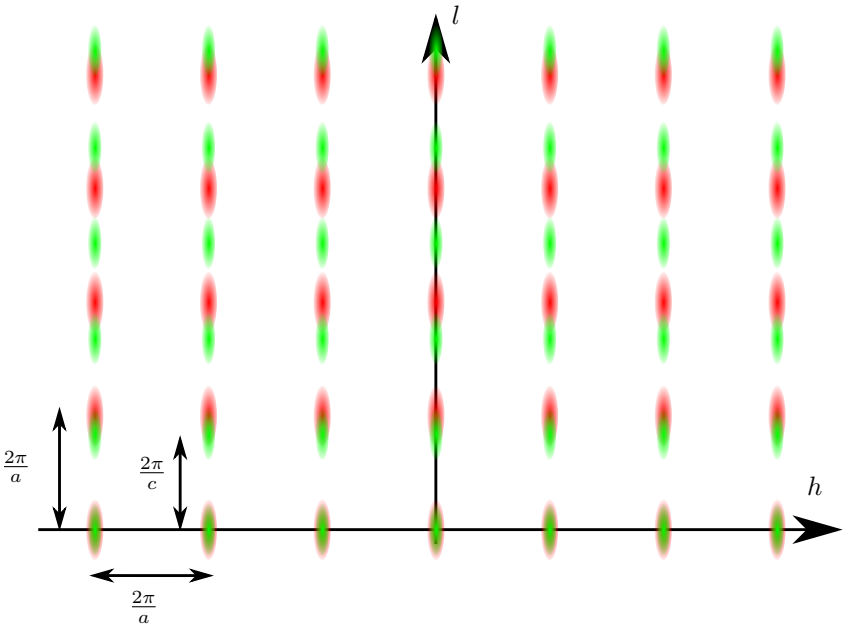

Figure 4.8: A sketch of the reciprocal space of an epitaxial tetragonal thin film on a cubic substrate. The reciprocal lattice points are spread out into truncation rods. Good epitaxy leads to the film (green) and substrate (red) peaks being aligned in-plane, indicating they have the same in-plane lattice constant. The out-of-plane lattice constant of the film is larger than that of the substrate, leading to closer lattice points.

For an infinite orthorhombic crystal with dimensions a, b, c, the reciprocal space will be a collection of points located exactly at $h\frac{2\pi}{a}, k\frac{2\pi}{b}, l\frac{2\pi}{c}$ with h, k, l integers. However, our samples are not infinite, and have an interface in the out-of-plane direction, leading to a smearing out of intensity along this direction in reciprocal space, called a crystal truncation rod. Another effect is that thin films only have a finite number of diffraction planes along the out-of-plane direction, leading to modulations in intensity with a period of $\frac{2\pi}{N_z c}$, called finite size oscillation. Moreover, the diffraction conditions will be different for the substrate and the film, leading to a superposition of the reciprocal spaces of both. Fig. 4.8 illustrates this schematically.

We are now in a position to interpret $(0, 0, l)$ scans and reciprocal space

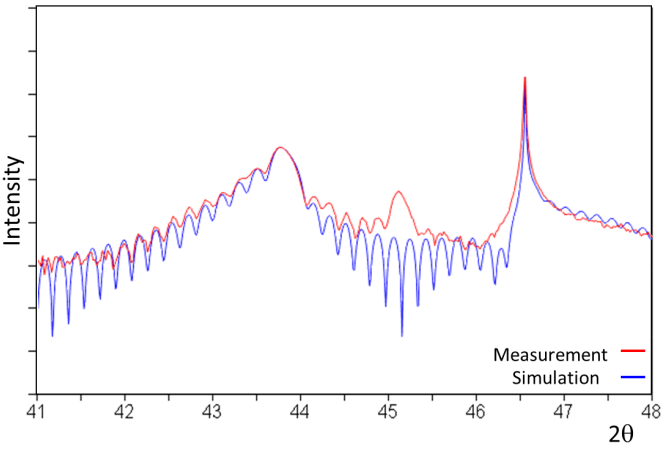

Figure 4.9: Example of a $(0, 0, l)$ scan (red) around the $(0, 0, 2)$ peak of both the film and the substrate with its fit (blue). We can see that the peak position and the finite size oscillations are well reproduced by the fit, allowing us to measure the (distribution of) c-axis and the thickness of the film respectively. The one peak not reproduced by the fit is exactly at the position where a double diffraction effect is expected according to [83].

maps. In $(0, 0, l)$ scans (see Fig. 4.9 for an example), θ and ω are scanned at the same rate with no offset. The resulting pattern shows the crystal truncation rod of the substrate, along with a film peak and its finite size oscillations. The position of the film peak informs us about the c-axis of the film, by inverting the Bragg condition to find $d_{00l} = \frac{c}{l} = \frac{\lambda}{2 \sin \theta}$. The period of the finite size oscillations can be used to find the thickness of the sample, and therefore the number of layers it contains. Both these parameters can be readily extracted from a simple fit based on the Bragg condition. However, to also take into account asymmetries in the peak shape, a more complex fit allowing c-axis variations through the film thickness is necessary. Such an approach, based on exponential c-axis distribution, was implemented in a *Matlab* program developed in house [84], and allows the shoulder of the sample $(0, 0, 2)$ peak to be fitted, as shown in Fig. 4.9.

For reciprocal space maps, the diffractometer is first set up to image a peak, and then a 2 dimensional slice of reciprocal space is measured by scanning both 2θ and ω in sequence. Reciprocal space maps will typically be used to probe off-specular peaks, that is peaks with h and/or k different from 0. This way, the position of the peak also informs us about the in-plane lattice parameter(s), and in particular we can check whether the sample is constrained, that is whether it has adopted the in-plane lattice parameter

of the substrate. If this is the case, the peaks due to the substrate and the sample will be aligned in the h and k directions.

It is possible for the Ewald sphere to contain more than one reciprocal lattice point. In this case, the incoming intensity will be diffracted in both directions, even if the detector is only set up to probe one of them. The diffracted intensity from the planes (h_1, k_1, l_1) may then serve as a new incoming beam for a second diffraction into the other available direction, (h_2, k_2, l_2). This diffraction will then seem to come from planes with the index $(h_1+h_2, k_1+k_2, l_1+l_2)$. As long as (h_1, k_1, l_1) and (h_2, k_2, l_2) are from the same reciprocal lattice, the doubly diffracted beam will be absorbed by another lattice reflection. If, however, they are from two different lattices, which can be the case for our heteroepitaxial thin films, a new peak will appear that is part of neither reciprocal lattice [85]. Typically, the beam will be diffracted in the substrate, and then again in the film. For the diffracted intensity from this weaker incoming beam to be detectable, the film must be sufficiently coherent, which is why we typically only detect these peaks in our highest quality thin films. The positions where these extra peaks are expected have been calculated in [83], and an example can be seen in Fig. 4.9, close to $2\theta = 45°$.

4.3 Second Harmonic Generation

Second harmonic generation (SHG) is a non-linear optical microscopy technique in which a strong laser source is used to excite an optical response at twice the frequency of the incoming light. Generally, an oscillating electrical field passing through a dielectric material will generate an oscillating polarisation, which in turn will propagate the electrical field further. To first approximation, the generated polarisation is linearly dependent on the incoming field. However, for materials without a centre of inversion symmetry, such as ferroelectrics, non-linear effects allow frequency doubling. These non-linear effects can become particularly important for strong electrical fields, such as they can be generated using a powerful laser. Microscopically, this corresponds to more than one photon coupling together to produce an oscillating polarisation at a multiple of the incoming frequency. In SHG, we analyse the response at exactly twice the incoming frequency, and are therefore sensitive to processes involving two incoming photons.

The power of SHG comes from the fact that the second order electrical susceptibility, which is the coupling tensor between the incoming light and the generated polarisation at twice the frequency, is heavily constrained by material symmetry. Thus, detecting an SHG signal is a strong indication about the symmetry of the probed region.

The SHG setup used in this work, described in Ref. [69], was developed

by S. Cherifi-Hertel at the Institut de Physique et Chimie des Matériaux in Strasbourg. It uses a pulsed laser with a wavelength centred at 800 nm, which is then focused on the surface of the sample using a confocal microscope at normal incidence, reaching a beam width of the order of 300 nm. The reflected light is then filtered and collected into a photomultiplier to record the intensity. The sample can be scanned along the x and y axes to image regions on the order of 10×10 µm^2 in steps of the order of 100 nm. The incident light is first linearly polarised to a certain angle ϕ, and the emitted light is then filtered by an analyser at an angle α, where both ϕ and α are measured counterclockwise from the x axis.

One key consequence of using a beam at normal incidence is that only an in-plane symmetry breaking can produce SHG signal in this configuration. Indeed, the second order electrical susceptibility is a third rank tensor, and therefore must be zero along axes that present inversion symmetry. Since the electrical field associated with a beam at normal incidence is completely parallel to the surface of the sample, there can only be SHG signal if there is a breaking of inversion symmetry along the in-plane axes. In a perfect Ising wall in a tetragonal ferroelectric with an out-of-plane polarisation axis, the in-plane centrosymmetry is not broken, which leads us to expect no SHG signal. However, if instead the wall has components of Bloch or Néel rotations (see Sect. 2.2.4), there will be SHG signal exactly at the wall, polarised in a predictable fashion. For domain walls that run along the x or the y axes, if the polarisation of the incoming beam (the angle ϕ) is either along the x or the y axes, the resulting SHG signal is polarised along the direction of the polarisation at the wall, that is parallel to the wall for Bloch walls and perpendicular to the wall for Néel walls. For the full derivation of this result, the interested reader is directed to Ref. [69] and its supplementary materials. This results in an easy way to distinguish between Néel, Bloch, or Ising walls in a tetragonal ferroelectric, which is what was done in Ref. [69] for $Pb(Zr_{0.2}Ti_{0.8})O_3$, finding Néel walls in this compound.

4.4 Off-axis radio frequency magnetron sputtering

Sputtering is a class of physical vapour deposition techniques. Argon ions are accelerated towards a target of the material to be grown, which is typically in ceramic form, where they collied and eject atoms of the target material. These adatoms then fly out in all directions inside the deposition chamber. The pressure inside the chamber is controlled in such a way that the secondary electrons from the collisions of the adatoms with the process gas maintain the plasma. When the adatoms reach the substrate, they condense, forming the film layer by layer. Sputtering techniques can be further subdivided by

the mechanism used to accelerate the ions (direct current (DC) vs radio frequency (RF)) and how the substrate is positioned with respect to the target (on- vs off-axis). Furthermore, a magnetron can be used to trap the secondary electrons close to the target, increasing the plasma density at this point and therefore the sputtering rates.

The device providing the voltage and power needed to ionise the argon gas and accelerate the ions toward the target is called a sputtering gun. It extends inside the vacuum chamber on which it is mounted, and the target is placed at the end. For metallic materials, a DC bias can be applied between the target and the walls of the chamber, which are grounded. This bias will then both ionize the gas inside the chamber, and accelerate the ions towards the target. However, to deposit insulating materials, such as those used in this study, this method cannot be used, since the target would be rapidly charged. The solution to this problem lies in applying an alternating bias at high enough frequency to short the capacitive barrier of the target. Indeed, these high frequency RF fields change sign fast enough that the ions do not have time to accelerate significantly in either direction. The electrons, however, are light enough to "follow" the field, leaving ionized gas in the chamber. The ions are then accelerated towards the target by a geometric effect: since the two terminals between which the field is applied are of very different size, one being the tip of the gun and the other being the whole inside surface of the deposition chamber, the density of electrons during the half cycle where they are close to the gun is much higher than during the other half cycle. This creates a net DC field for the ions, which are then accelerated towards the target.

The material ejected from the target will diffuse in every direction, but the highest flux is achieved normal to the target. This means that placing the substrate across the gun in the chamber (on-axis) will yield the highest deposition rate. However, this also means that high energy adatoms coming directly from the target, as well as negatively charged ions present in the process gas, may hit the forming film and cause back-sputtering, which will introduce disorder in the sample. For complex oxides, it has been shown that the stoichiometry of the sample will not be uniform for on-axis growth [86]. The solution is to place the substrate at a 90° angle with respect to the normal to the gun. This will drastically reduce deposition rate, but ensure uniform stoichiometry and very coherent films.

At this point, it is worth noting that the rate at which individual atomic species are extracted from a target by the argon ions is not necessarily the same. However, since the adatoms are extracted from the surface, after sufficient time an equilibrium state is reached where the species with a higher extraction rate are less present at the surface, and the mix of atoms released in the chamber is equivalent to the stoichiometry of the target. It is important to reach this equilibrium before deposition, which can be done by

a process called "presputtering", where the deposition process is run with no substrate for several hours before using a new target, or new conditions, for deposition. Another thing to consider is that some elements with high volatility may diffuse out of the growing sample if a sufficient partial pressure is not present in the chamber. Most notably, to grow oxide materials, oxygen has to be added along with the argon in the process gas. It is also common to use targets with excess stoichiometry for very volatile elements, namely lead and bismuth in this study.

The samples used in this study where all grown by off-axis RF magnetron sputtering, in the chamber described in detail in Ref. [87]. Before deposition, the substrate is pasted on a resistive heater using silver paste, and then mounted in the chamber, which is pumped down to a base pressure of around 5×10^{-7} mbar. Argon and oxygen are then introduced at a constant flow rate, and the pressure inside the chamber set using a butterfly valve. The substrate is then heated to the growth temperature, as determined by a thermocouple inside the resistive heater, before opening the shutter in front of the target to be used and applying the chosen RF power. This procedure shows the many parameters which need optimisation to achieve optimal growth conditions: the ratio of argon to oxygen in the process gas, the overall deposition pressure, the deposition power, and the growth temperature. All of these parameters except the growth temperature may also influence the rate at which atoms are sputtered off the target, and therefore any change to one of these parameters requires a new presputtering.

Let us also note at this point that our chamber is not equipped for any in-situ growth monitoring technique, such as reflection high-energy electron diffraction (RHEED) which is common for other physical vapour deposition techniques. Indeed, making RHEED compatible with the high pressures inside the chamber and the high magnetic and electrical fields used during sputtering requires highly specialised equipment and a carefully crafted chamber geometry. All our sample are therefore characterised after growth, by x-ray diffraction to determine their crystalline quality, AFM to quantify their surface roughness and morphology, and PFM to probe their intrinsic polarisation state.

CHAPTER 5

Effect of growth temperature on post growth polarisation state

We have seen in Sect. 2.2 that the control of the polarisation state is a long-standing technological and fundamental challenge. Ideally, what is needed is a mechanism allowing full deterministic control over the intrinsic polarisation state, from one monodomain state, through polydomain, to the other monodomain state, reliably, robustly and in general under the different electrostatic and environmental boundary conditions which the sample would encounter during device fabrication and use.

In this chapter, we report such full control over the intrinsic polarisation of epitaxial thin films of the canonical ferroelectric $PbTiO_3$ (PTO, see Sect. 2.1.2 and following), showing that a monodomain "up", polydomain, or monodomain "down" state can be established as a function of increasing growth temperature, under full biaxial strain with no relaxation, independently of the choice of electrostatic boundary conditions, and ex-situ stable for at least two years. We demonstrate this extremely robust control in four series of samples with different back electrodes, grown at a range of temperatures and characterised by piezoresponse force microscopy (PFM, see Sect. 4.1.2), x-ray diffraction (XRD, see Sect. 4.2), and Rutherford backscattering (RBS), a technique which allows us to probe sample stoichiometry. Our measurements reveal Pb-vacancy gradients and a variation of unit-cell length (c-axis) across the film thickness. Our results are consistent with a microscopic mechanism of a growth temperature driven effective internal field during growth, which induces a gradient of divacancy (Pb-O) dipoles.

After the growth is completed, these dipoles result in a varying built-in field across the film, which then stabilises the target polarisation state.

Since this Chapter was written, new evidence has come to light which challenges some of its conclusions. The reader is therefore directed to Ref. [88] for complementary information.

5.1 Initial PFM observations

Using off-axis radio-frequency magnetron sputtering (see Sect. 4.4), four series of 50 nm thick $PbTiO_3$ samples were epitaxially grown on (001)-oriented $SrTiO_3$ single-crystal substrates, either Nb-doped or undoped and with a bottom electrode of $LaNiO_3$ or $SrRuO_3$, the latter in one series capped with an additional thin $SrTiO_3$ layer to modify the depolarising field, as schematically illustrated in Fig. 5.1. For each series, the deposition conditions were kept the same, except for the growth temperature, which was varied between 530°C and 590°C. For detailed growth conditions, see Appendix A. Due to their low thickness and the negligible in-plane lattice mismatch between the $SrTiO_3$ substrate and the a axis of tetragonal $PbTiO_3$, all samples were fully strained, as demonstrated by reciprocal space XRD maps (see, for example, Fig. 5.2), with no indication of relaxation of the in-plane lattice parameter. The slight bi-axial compressive strain ensured that the tetragonal c axis was out-of-plane, meaning that so was the polarisation of all films, with only two orientations possible: up (pointing away from the substrate) or down (pointing toward the substrate).

In each sample, the intrinsic polarisation state was investigated and compared to a well defined artificial domain structure of alternating down/-up/down/up/down stripes written with a biased scanning-probe microscope tip. As can be seen in Fig. 5.1 the four series all present the same trend, independently of the choice of bottom electrode: samples grown at lower temperatures are fully up-polarised, and samples grown at higher temperatures are fully down-polarised, with a polydomain state for intermediate growth temperatures. While previous studies have demonstrated that an intrinsically monodomain polarisation state is direct evidence of an internal bias in the sample [28], favouring one polarisation over the other, only one of the two possible monodomain states was ever stabilised for a given choice of electrode and film thickness. In contrast, the robustness of the phenomenon observed here indicates that independently of interface effects, the internal bias changes sign solely due to growth temperature.

To further investigate this change in the internal bias, we performed switching spectroscopy PFM (SSPFM, see Sect. 4.1.2) measurements of the local polarisation-voltage hysteresis at multiple points in each sample. The built-in voltage, defined as the shift of the hysteresis loop with respect

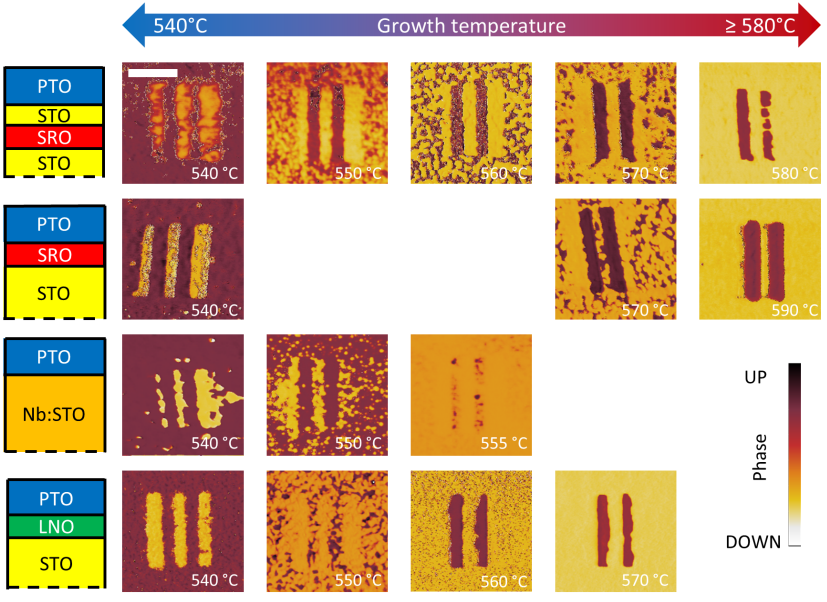

Figure 5.1: PFM phase for samples grown at different growth temperatures for various back electrodes. The white scale bar in the upper left image is 400 nm and is valid for all images. The direction of background polarisation was determined for each sample by writing striped domains of know orientation. Samples in the same column were deposited at temperatures within 5 °C from each other. The back electrodes used were, from top to bottom : 22 nm of $SrRuO_3$ (SRO) caped by 2 nm of $SrTiO_3$ (STO), $SrRuO_3$ without the capping layer, the conductive Nb:$SrTiO_3$ substrate, and 8 nm of $LaNiO_3$ (LNO). All electrodes and capping layers were deposited in-situ. In each series, the as-grown polarisation state follows the same trend: monodomain up for low growth temperatures, polydomain for intermediate growth temperatures and monodomain down for high growth temperatures.

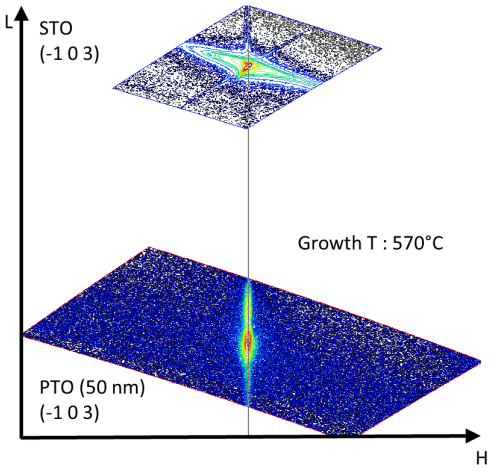

Figure 5.2: Reciprocal space map of a representative sample grown on LNO, around the (-1 0 3) peak of the substrate and the PTO film. The well defined sample peak attests of the high crystalline quality of the sample, whereas the fact that it is perfectly aligned in the H direction with the substrate peak indicates that there is no relaxation.

to zero bias, was extracted for each of these points and used as statistical estimate of the internal bias. The variation of the built-in voltage, presented in Fig. 5.3 as a function of growth temperature for the representative series of samples on $LaNiO_3$ back electrode, indeed shows a significant decrease, changing sign from positive at lower growth temperatures to negative for higher growth temperatures, in agreement with the PFM phase imaging results.

5.2 Post growth in-situ annealing

To better understand the origin of this phenomenon, we then tested if the high-temperature vs. low-temperature polarisation state was only established during growth, or if it could be modified subsequently using temperature alone. We grew a series of samples at low growth temperature (545 °C, corresponding to a monodomain up configuration) which were then heated for varying times to 570 °C, the temperature corresponding to a monodomain down configuration, in situ after completion of the growth process. As Fig. 5.4 shows, even after a very short heating time, down polarised domains appeared in the up polarised matrix. For a sufficiently long heating time, a down polarised state was achieved. This suggests that the duration of the sample exposure to high temperatures under process conditions is more

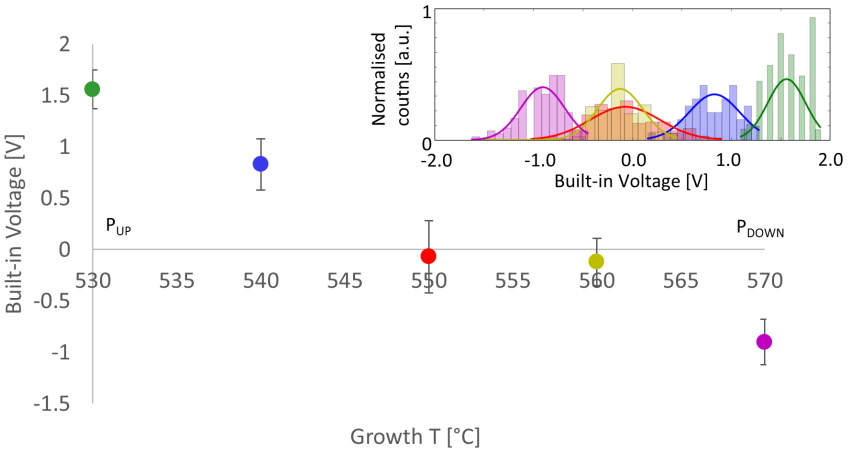

Figure 5.3: SSPFM measurements of built-in voltage in each sample of the series grown on $LaNiO_3$. The inset shows the distribution of shifts of local hysteresis loops with respect to the origin for each sample, and Gaussian fits to that data. The main graph shows the fitted averages and standard deviations. The built-in voltage goes from positive at low growth temperature, which favours the up polarised state, to negative at high growth temperature, which favours the down polarised state, in line with our PFM imaging results.

critical to the intrinsic polarisation state than the fact that this exposure happens specifically during growth.

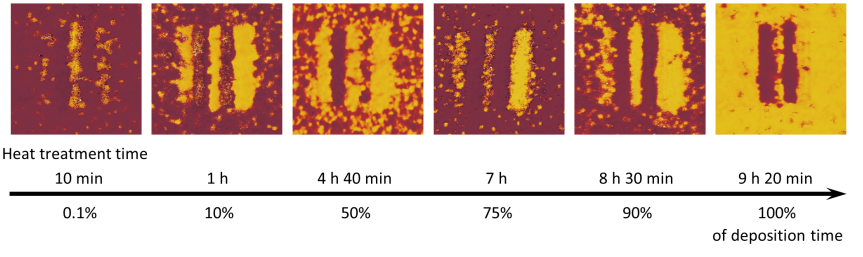

Figure 5.4: PFM images of samples grown at a low growth temperature (corresponding to a monodomain up polarised state) and subsequently heated to a higher temperature (corresponding to a monodomain down polarised state) in situ for various durations. The usual control pattern was written in the centre of the images. Even for very short heating times (with respect to the total deposition time of 9 hours and 20 minutes), the samples exhibit some down domains. After a sufficiently long heating time, a down polarised state is achieved. This suggest that we can control the intrinsic polarisation state by heating the samples in low pressure.

5.3 Stoichiometry variation measured by RBS

Chemical species mobility depends exponentially on temperature [89]. Compositional changes and gradients have also previously been shown to produce large built-in fields [90]. To explore the potential presence of compositional gradients, the stoichiometry of our films was measured through their thickness using RBS by L. R. Dedon under the supervision of L. W. Martin at the University of California, Berkeley. Spectra were taken on a series of 5 samples grown on an 8 nm $LaNiO_3$ electrode at temperatures ranging from 530 to 570°C in 10°C intervals (see Fig. 5.5). This thickness of electrode allowed us to distinguish between signal from the film and the substrate. Each spectrum was then fitted to extract an average stoichiometry using the SIMNRA software [91], keeping titanium as a constant reference, since it is expected to be much less volatile than lead. The results are shown in Fig. 5.5. The same spectra were then fitted again using this time four "slices" of varying composition throughout the thickness of the sample. The stoichiometry of the top- and bottom-most slices are shown in Tab. 5.1. As can be seen in Fig. 5.6(a), these fits reveal that the average Pb content diminishes with increasing growth temperature, going from 16% over-stoichiometric, slightly exceeding our 10% Pb-rich target stoichiometry, to 7% Pb deficient. The observed Pb distribution moreover appears to be inhomogeneous through the film thickness, as can be seen in Fig. 5.6(b), with the top surface showing higher levels of Pb deficiency for high growth temperatures, suggesting a gradient in Pb vacancy concentration.

Growth temperature [°C]	Pb:Ti Top	Pb:Ti Bottom
530	1.16	1.14
540	1.02	1.02
550	0.95	0.98
560	0.93	0.96
570	0.90	1.00

Table 5.1: For each of the samples shown in Fig. 5.5, this table shows the growth temperature and the fitted stoichiometry for the slice closest to the surface and closest to the interface, out of four slices throughout the thickness of each sample.

5.4 The microscopic model

Taken together, these results allow us to discriminate between the different microscopic mechanisms that could potentially contribute to the observed growth temperature dependence of the intrinsic polarisation orientation.

First of all, we note that deposition temperature is one of the most important parameters for growth optimisation, with significant effects on the

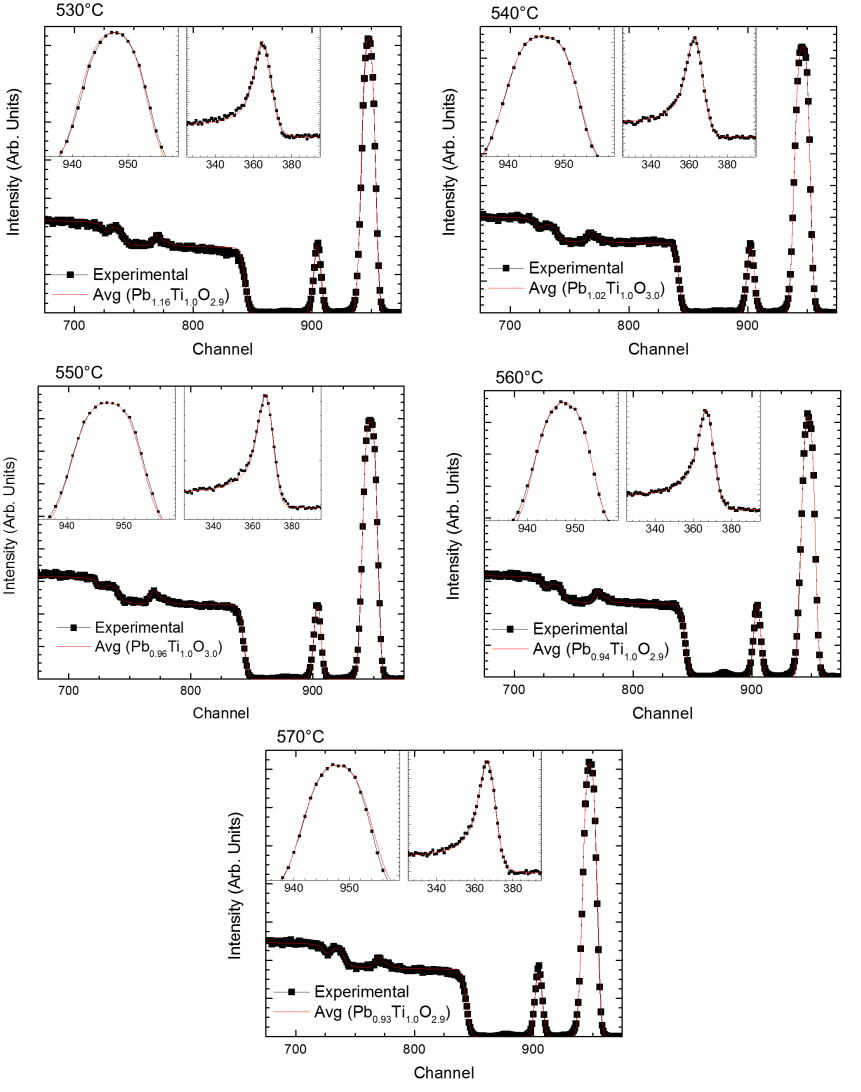

Figure 5.5: RBS spectra for each of the samples in a series on LNO. The black dots indicate data points and the red curve the profile simulated with the average composition given on the figure. The insets show a magnification of the peak due to lead (left) and oxygen (right).

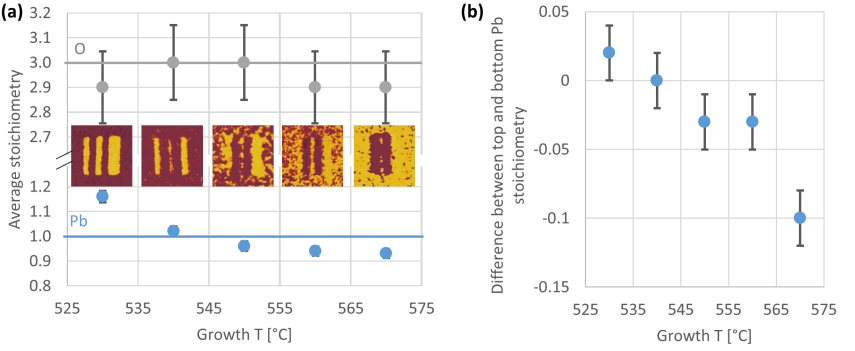

Figure 5.6: (a) Average lead and oxygen content in the five samples measured by RBS, as shown in Fig. 5.5. Titanium was assumed to always be stoichiometric and used as a reference. Error bars represent the uncertainty of the fit. The insets show the PFM phase image for each sample, with the control down/up/down/up/down structure written in the middle of the imaged area. Low temperature grown samples are monodomain up, and up to 16% over-stoichiometric in lead, whereas high temperature grown samples are mostly down polarised, and up to 7% lead deficient. Note that the target used was 10% lead rich. This indicates that lead vacancies favour the down polarised state. RBS is less sensitive to lighter elements, explaining the much larger error bars on the oxygen stoichiometry - these measurements cannot exclude oxygen vacancy densities of the same order as the lead vacancy densities. b) Difference in lead stoichiometry between the top (close to the surface) and the bottom (close to the interface with the electrode) of the $PbTiO_3$ thin films, as a function of growth temperature. Low growth temperature samples are homogeneous within the experimental error, whereas high growth temperature, down polarised samples have significantly less lead at the surface.

quality [86] and potentially the polarisation of the resulting films. In our case, there are indeed some variations in the crystalline and surface quality across the temperature range, however, for the sample series on Nb:$SrTiO_3$, where the reorientation of the as-grown polarisation from up to down occurs over the narrowest temperature range (540 to 555°C), consistently high crystalline and surface quality was shown by XRD spectra and surface topographies (see Fig. 5.7), thus demonstrating that variations in sample quality cannot trivially account for the observed effect.

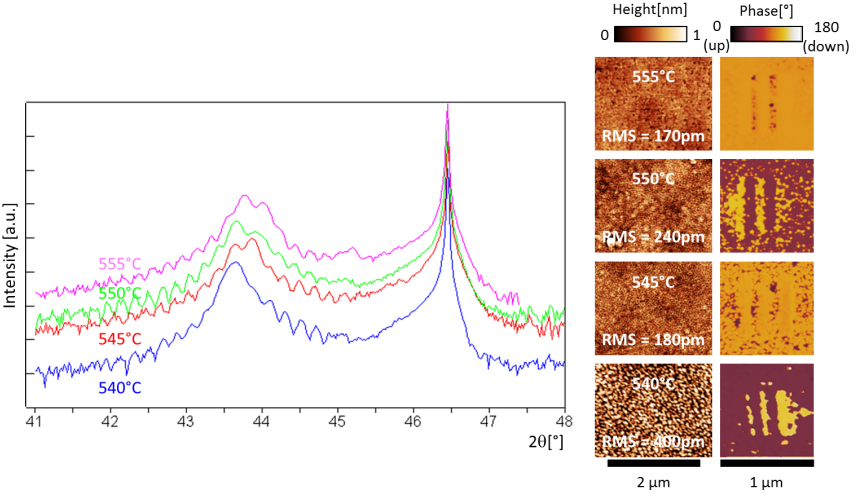

Figure 5.7: From left to right: X-Ray diffractograms around the (002) reflection, showing Laue oscillations attesting to the high crystalline quality of the films; surface topography (with root mean square (RMS) roughness indicated), in each case the RMS roughness is below one unit cell; and PFM phase images including the written control structure of four samples of the series on Nb:STO, grown in a window of temperatures of 15 °C between 540 °C and 555 °C. These samples all show very high quality, but the as-grown polarisation nonetheless changes orientation over this very narrow range of temperature.

In Ref. [92], Selbach *et al.* propose a model where Pb vacancies and their compensating O vacancies separate to screen the bound charge. This is incompatible with our RBS results, since Pb vacancies are a negatively charged defect, and simple electrostatics suggest that they should therefore accumulate at the bottom interface of a down polarised film, not at the top surface as we see here. It is however reported [93, 94] that Pb vacancies are able to form a dipolar divacancy complex with O vacancies, the presence of which is not excluded by the RBS data, and indeed highly probable in perovskite oxide thin films [95]. If we therefore consider the RBS measurements as a marker not simply for Pb-vacancies, but for Pb-O divacancy

complexes, these would appear to be more present in down polarised films. Our previous work meanwhile suggests that an external built-in field due to the asymmetry of electrostatic boundary conditions favours an up polarised state at room temperature [28]. We could therefore infer that the divacancy complexes stabilise the down polarisation in films which would otherwise be up polarised due to an external built-in field. This mechanism is schematically summarised in Fig. 5.9(a).

A possible explanation as to why the defect dipoles would oppose the external built-in field at room temperature is that the built-in field present during growth is very different. Indeed, Highland *et al.* have shown [40, 96] that the equilibrium polarisation of $PbTiO_3$ thin films depends on temperature and oxygen partial pressure. Most notably, for partial pressures close to the 0.1 mbar that we use during growth, both polarisation orientations can be stable depending on temperature, see Fig. 2.9. It is also generally accepted that Pb-O divacancy dipoles do not change direction after they have been formed, contributing to the built-in field (see, for example, references [37, 97]). Therefore, we believe that the divacancy dipoles can be engineered to "freeze in" the polarisation state present during growth.

5.5 Determination of the c-axis distribution in the films

One key consequence of this model is that, since the divacancy dipoles are not present everywhere in the same concentration, the internal field the sample is subject to also varies locally. Since this internal field is coupled to the out-of-plane *c*-axis of the unit cell through the polarisation, we are able to measure a corresponding gradient in the *c*-axis. To investigate this, transmission electron microscopy (TEM) measurements, which allow us to resolve single atomic columns in a thin cross section prepared by ion beam milling, were performed on a series of three samples grown on 4 nm of $LaNiO_3$ and polarised up, down, and in a polydomain state, respectively, by A. B. Naden at the Queen's University Belfast. The TEM images were then analysed using geometric phase analysis (GPA) [98, 99], a reciprocal space technique that reveals local changes in lattice parameters. The images (see Fig. 5.8) once again confirm a high crystalline quality and epitaxy throughout the growth temperature range. However, within the resolution of ± 2 pm of these experiments, the GPA analysis did not allow us to see any significant changes in the *c*-axis between the top and the bottom of our films.

We therefore turned to a finer, although indirect, method to extract the lattice parameters of our films: XRD measurements, which were taken for all our samples as part of our standard initial characterisation, providing a significant data set for cross-comparison. In all cases, the down polarised

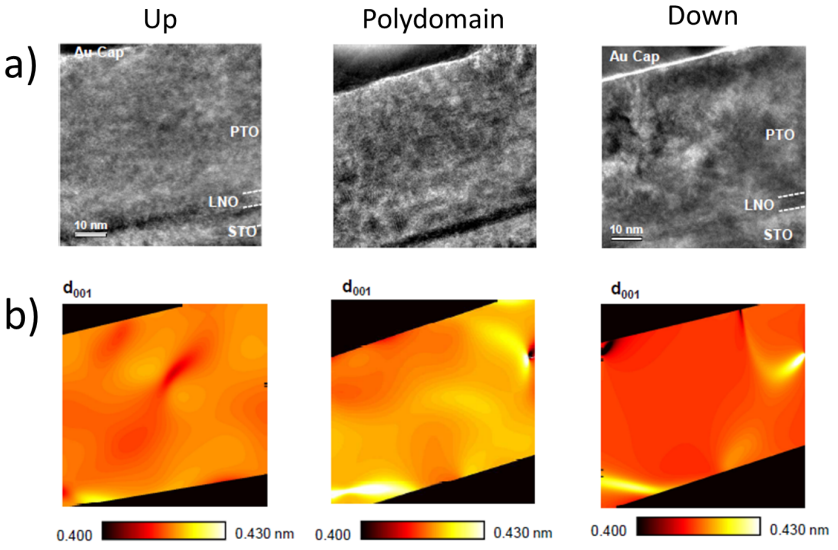

Figure 5.8: (a) HRTEM images of three PTO samples grown on LNO, with intrinsic polarisation state up, down and polydomain respectively. We can again see that all the samples have high crystalline quality, independently of growth temperature/intrinsic polarisation state. The mottled contrast is due to variations in lamellae thickness. (b) GPA phase images show no significant variations in lattice parameter within the experimental error. Some phase deconvolution artefacts show at the edges, where lattice fringe visibility was low.

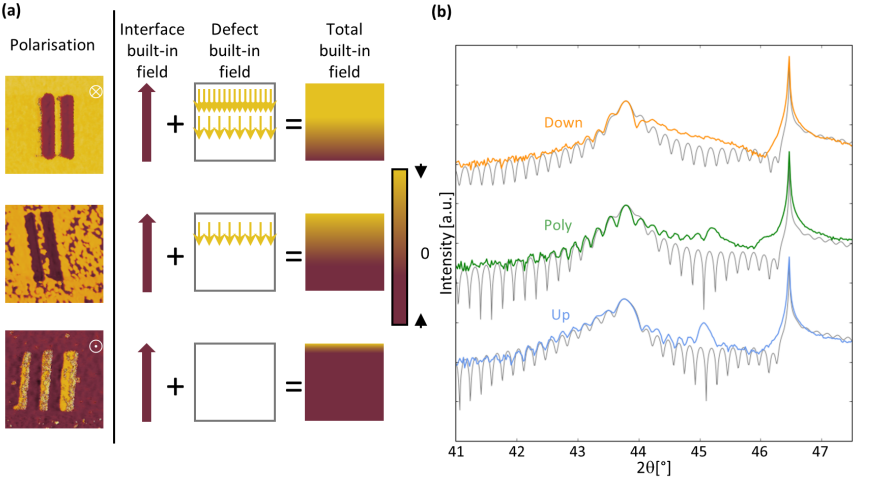

Figure 5.9: (a) The proposed model: a built-in field due to the interfaces favours the up polarisation, and measured lead-vacancies form lead-oxygen defect dipoles that favour the down polarisation. The sum of these contributions produces an inhomogeneous effective built-in field throughout the sample. (b) Example of $\theta - 2\theta$ XRD patterns around the (002) peak of both the film and the substrate, for three films on LNO, respectively polarised monodomain up, polydomain, and monodomain down. As in all our series, the high temperature grown, down polarised film shows a distinctive shoulder to the right of the sample peak, distinct from the very sharp double diffraction peak [83, 100] present in the other samples close to $2\theta = 45.3°$ (not reproduced by the fit), indicating a small region of lower than average c-axis in those films. Spectra fitted to the data are shown in grey.

samples presented a shoulder on the right side of the main film diffraction peak - indicating a region of lower c-axis - which we did not observe in the up polarised samples (Fig. 5.9(b)). In fact, in many cases, the up polarised samples present a spectral weight to the left of the main film diffraction peak.

As can be seen in Fig. 5.10, fitting our typical XRD spectra using a constant c-axis distribution throughout the thickness of the sample does not capture many of its more interesting features, namely the broadening and asymmetry of the peak. Following the argument in [101] that any mechanism to relax strain would depend on strain, the next reasonable level of complexity is an exponential distribution of the form $c(n) = c_0 + a\exp(n/b)$, where $c(n)$ is the c-axis of the n^{th} unit cell above the interface with the electrode. This was done using a *Matlab* program developed in-house [84], and the results are shown on Fig. 5.10. Note that this program does not simulate peaks due to double diffraction [83, 100] which appear close to $2\theta = 45.3°$ in Fig. 5.9(b). This fit captures the main features of the diffractograms much better, with very different c-axis distributions in the up vs. down polarised films (Fig. 5.11(a)). The coefficients used for those two samples can be found in Tab. 5.2. Note that one can obtain $c(z)$, the c-axis at a distance z above the interface with the electrode with minimal error by letting $n = z/\bar{c}$, where $\bar{c}$ is the average c-axis throughout the thickness of the sample. For large parts of the sample, the variation in c-axis is below the resolution of our TEM measurement which is about 2 pm. This method therefore allows us to probe much smaller variations than TEM.

Polarisation	a[Å]	b[u.c]	c_0[Å]	$\bar{c}$[Å]
up	0.000275	23	4.12493	4.140
down	-0.061	-110	4.16662	4.130

Table 5.2: Coefficients of the expression $c(z) = c_0 + a\exp\left(\frac{z}{b\bar{c}}\right)$ for two typical monodomain samples, one up polarised, one down polarised. Note that only three of the coefficients are independent for each sample, since $\bar{c}$ is the average c-axis throughout the sample.

5.6 The relationship between polarisation and strain

To estimate the polarisation inside our films, we used a Gibbs free energy expansion to link the strain profile obtained from these fits to the polarisation inside our films. We will focus on the monodomain end members of our study, and therefore neglect the effects of in-plane inhomogeneities of the polarisation present in polydomain samples.

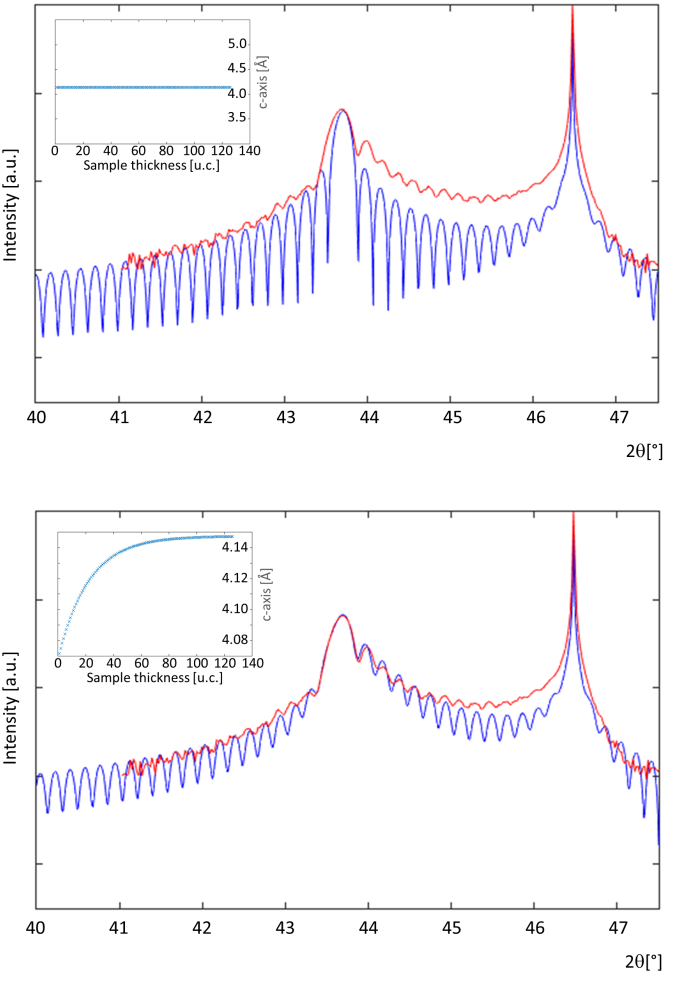

Figure 5.10: A typical diffractogram around the 002 peak of one of our samples (LNO back electrode, 540°C growth temperature), along with the best fit assuming a constant c-axis throughout the film and an exponential distribution of c-axis, respectively. The c-axis profile used for each fit is shown in the inset. The fit using the exponential distribution much better captures the main features of the diffractogram, namely the "shoulder" on the right side of the sample peak.

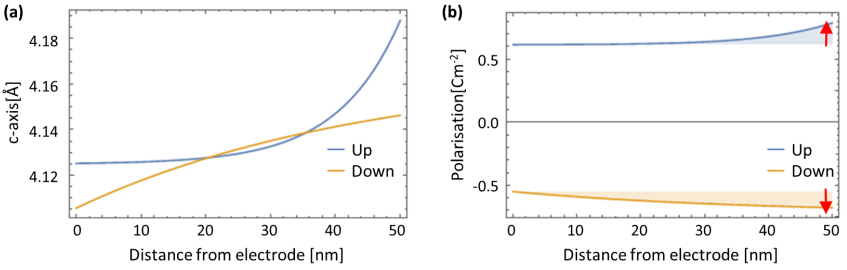

Figure 5.11: (a) c-axis distribution obtained from the fit to the XRD spectra of the up and down polarised samples in Fig. 5.9(b). (b) Polarisation profiles for the samples in (a) obtained from the GDL calculation using the c-axis profiles in (a). The red arrow indicates the polarisation due to the defect dipoles estimated using the RBS data and values from the literature (see main text). We see that the variations inside the film are of the order of magnitude expected for the measured density of defect dipoles.

Traditionally, to get the polarisation in a film from information about its strain state, we invert the electrostriction term in the expression for the strain obtained using the Gibbs free energy expansion to get

$$P_3 = \pm\sqrt{\frac{1}{q_{11}}(c_{11}e_3 + 2c_{12}u_m)} \tag{5.1}$$

where P is the polarisation, e_i is the strain (in Voigt notation), c_{ij} is the stiffness tensor, u_m is the mismatch strain with the substrate, and q_{ij} is the electrostriction tensor. However, this expression does not take into account the effect of inhomogeneity in the strain, which is present in our films, and can significantly change the polarisation through flexoelectric coupling. We therefore try to rederive this expression starting with the full Gibbs free energy. Picking up where we left in Chapter 3, we have

$$\begin{aligned} G = \int_0^t [&a_3P^2 + a_{33}P^4 + a_{333}P^6 \\ &+ \frac{1}{2}c_{11}(2u_m^2 + e_3^2) + c_{12}(u_m^2 + 2u_m e_3) - q_{11}e_3P^2 - 2q_{12}u_m P^2 \\ &+ \frac{g_{1111}}{2}\left(\frac{\partial P}{\partial z}\right)^2 - \frac{f_{11}}{2}\left(P\frac{\partial e_3}{\partial z} - e_3\frac{\partial P}{\partial z}\right) \\ &- PE - 2\sigma u_m]dz \end{aligned} \tag{5.2}$$

where, in addition to the quantities defined above, g_{ij} is the correlation energy tensor, f_{ij} is the flexocoupling tensor, σ is the in-plane stress the sample is subject to, and E is the electrical field the sample is subject to (including the depolarising field). Applying Eq. 3.13 with $A = e$ yields

$$c_{11}e_3(z) + 2c_{12}u_m - q_{11}P^2 + f_{11}\frac{\partial P}{\partial z} = 0 \tag{5.3}$$

which would lead back to Eq. 5.1 in the absence of flexoelectricity. Since we know $c(z)$ for each sample from the fits to their x-ray diffractograms, we can calculate $e_3(z) = \frac{c(z)-c_{ref}}{c_{ref}}$, with c_{ref} the c-axis of the non-ferroelectric reference phase, and solve Eq. 5.3 to find $P(z)$.

As explained in the previous section, we fit the c-axis throughout the sample by adjusting the parameters of the expression $c(z) = c_0 + a\exp\left(\frac{z}{b\bar{c}}\right)$. The coefficients for two typical monodomain samples, one up polarised, one down polarised, are given in Tab. 5.2. This leads to a simple functional form for $e_3(z)$, the strain throughout the thickness, allowing us to solve Eq. 5.3 for $P(z)$ in closed form using *Mathematica*. As a boundary condition, we used the value obtained using Eq. 5.1 at either interface. The results are shown in Fig. 5.12, where they are compared to the curve obtained by naively using Eq. 5.1 for every z value. We can see clearly that the inclusion of flexoelctricity (last term of Eq. 5.3) does not change the resulting polarisation distribution significantly.

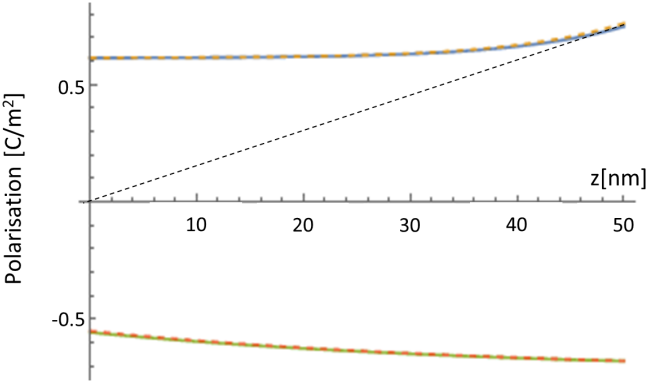

Figure 5.12: Polarisation profiles obtained from two typical strain measurements, using the full Eq. 5.3 (full), and the simplified form (Eq. 5.1, dashed). We see that the difference is minimal. The dashed black line indicates the polarisation distribution used to estimate the order of magnitude of each term in Eq. 5.3. We can see that the actual gradient is never larger than this.

To better understand why this term seems to have so little influence, let us estimate the order of magnitude of each term in Eq. 5.3. The values for c and q are taken from [15], whereas the value for f_{11} is take from [35]. u_m is calculated with respect to the cubic reference state. e_3 is measured to be of the order of 5% with respect to the same reference. The polarisation in this kind of thin film is known to be at most 0.8 C/m^2. To get an estimate of the

polarisation gradient, we assume that the polarisation drops linearly from this maximal value to 0 over the thickness of the film, which is a higher gradient than the maximal gradient observed in Fig. 5.12. Taking all of this together, we get, in S.I. units, that the first term is of the order of $8.7 \times 10^9\,\mathrm{J\,m^{-3}}$, the second term $-2.6 \times 10^9\,\mathrm{J\,m^{-3}}$, the third term $7.3 \times 10^9\,\mathrm{J\,m^{-3}}$ and the last term only $-2.7 \times 10^8\,\mathrm{J\,m^{-3}}$. The correction to the polarisation obtained by including this term is not very large, and we therefore prefer the closed form of Eq. 5.1, which is plotted in Fig. 5.11(b).

Note that within this derivation we do not take into account a change in the reference state due to the gradient in stoichiometry that was measured in RBS, which would lead to an effective strain gradient both in-plane and out-of-plane, as in [90]. Indeed, we can estimate this chemical strain gradient with the values measured in [92]. We find that the difference in strain for the largest measured change in stoichiometry would be of the order of 0.01% in-plane and 0.02% out-of-plane, 2 orders of magnitude lower than the strains already taken into account. This leads us to conclude that flexoelectricity does not play a big role in the effect we observe.

5.7 The contribution of defect dipoles to the polarisation

Eq. 5.3 is agnostic of any electrical fields the sample might be subject to, and returns the total polarisation, irrespective of what caused it. A built-in field coming from the interface is constant throughout the thickness of the film and results in a constant polarisation (and thus a constant c-axis). In our model, the variations in polarisation implied by the varying c-axis we measure come from the defect dipoles.

By definition, polarisation is the spatial density of dipole moments. The dipole moment of one divacancy complex can be calculated to be its effective charge, multiplied by the distance between the two vacancies. Since we are only considering out-of-plane polarisation, we will focus on the out-of-plane distance and assume the in-plane contributions cancel out. According to Ref. [94], the optimal position for the vacancies are next nearest neighbour, meaning the out-of plane distance is the c-axis times a factor that captures the shift of the oxygen octahedron with respect to the lead lattice, which is reported to be 0.88 in Ref. [102]. Cockayne and Burton [103] calculate the effective charge of such a divacancy to be $2.28e$, close to the naive ionic value of $2e$, although they operate with fixed atomic position and in a nearest neighbour configuration. These differences in set-up are however unlikely to drastically change the value obtained. Taking all of this together we obtain a dipole moment for one divacancy of $0.88c \times 2.28e$.

The density of these dipoles can now be estimated as the amount of

lead vacancies per unit cell measured by RBS. Using the lead vacancies as markers for divacancies, we get that the highest concentration of divacancies would be 0.1 per unit cell or $0.1/abc = 0.1/a^2c$ since the in-plane lattice parameter is given by the cubic substrate. Taking this together with the moment obtained above, we finally get $P \approx 0.88c \times 2.28e \times 0.1/a^2c \approx 0.2$ C/m^2. Although the assumptions made in these different sources do not necessarily correspond exactly to our experimental set-up, we believe this number to be a valuable order-of-magnitude check of our model. Indeed, as is shown in Fig. 5.11(b), the variation in polarisation calculated throughout the thickness of the sample is very close to this value.

5.8 Dependence on film thickness

To try to get an understanding of what happens during different stages of growth, we additionally analysed two series of three samples of different thicknesses, grown at low vs. high temperature, respectively. The reference sample in each series was the standard 50 nm thickness and the growth temperatures were chosen such that it was monodomain up for one series (low growth temperature) and monodomain down for the other series (high growth temperature). Each series was completed by a thinner sample (about 20 nm thick) and a thicker sample (about 100 nm thick). As Fig. 5.13 (c) shows, the thin, high growth temperature sample has a lower average c-axis than its reference and is polydomain. This can be viewed as a combined effect of both the depolarising field (see Sect. 2.2.1) and the lower density of defect dipoles due to the lower process time. The thin, low temperature sample, in contrast, is monodomain up in the same direction as its reference, although with a lower average c-axis. The thick, high temperature sample is monodomain down, and has a higher average c-axis than its reference, which could indicate that the polarisation is stabilised by a higher dipolar defect concentration. However, the thick, low temperature sample is polydomain, which can be explained by defect dipoles favouring the down polarisation having the time to form during the longer process time. Also, the results presented in Ref. [40] seem to indicate that for the same chemical environment, thicker films are closer to the down polarisation state. We see that these observations can be explained with our model: films that have little time to form defect dipoles are closer to an intrinsic up polarisation due to the built-in field from the interface. Thicker films are closer to a down polarisation during growth, and are exposed to the growth atmosphere for a longer time, leaving more time to form defect dipoles to stabilise this orientation.

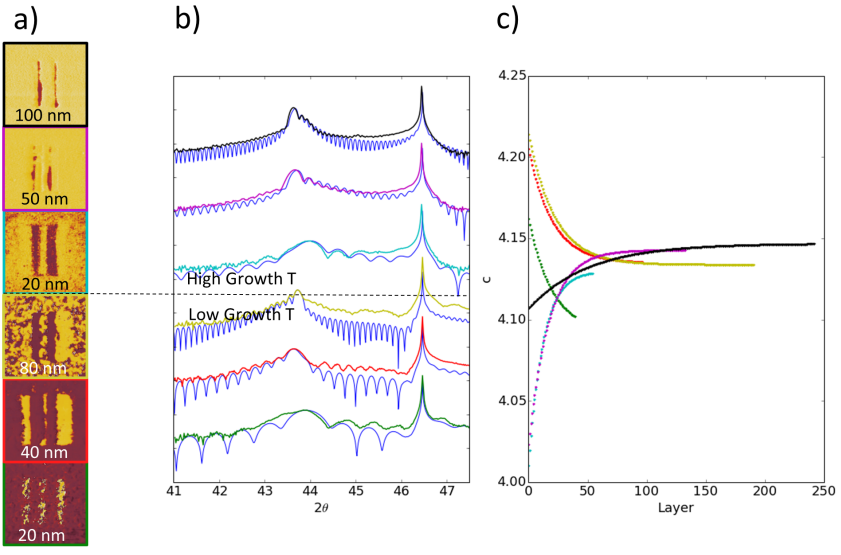

Figure 5.13: (a) PFM, (b) X-ray diffractograms, and (c) resulting c-axis profiles for two series of three samples of different thickness, grown at different growth temperatures. The growth temperature for each series was chosen such that the standard 50 nm thick sample was monodomain up (low growth temperature) or monodomain down (high growth temperature). The differences in c-axis and domain structures can all be explained using our model.

5.9 Diffractograms for higher temperatures

Finally, we analysed the diffractograms of two samples, grown at high and low temperature, respectively, while they were heated in air. For the high temperature sample, two peaks were tracked, corresponding to the high *c*-axis "main" peak and the low c-axis "shoulder" at room temperature. As Fig. 5.14 shows, although the separation between these two peaks remains approximately constant, spectral weight shifts from one to the other during heating, and back (although not completely) during cooling. Moreover, during heating of the low growth temperature sample, the same "shoulder" appears, and also takes over most of the spectral weight at high temperature. Notably, Laue oscillations reappear at this stage, denoting higher coherence than at lower temperature. We also see a kink in the *c*-axis curves of both samples at approximately 600°C, see Fig. 5.15, which indicates a phase transition from the ferroelectric to the paraelectric phase. If we compare the highest temperature diffractograms for both samples Fig. 5.16, we see that they no longer show differences in their main features. This could indicate that the "shoulder" at room temperature originates from a part of the sample in a state of lower polarisation, and that this part grows as the sample is

heated until the polarisation disappears in most of the sample, which would also explain why the ferroelectric transition is not as sharp as expected. However, it seems that part of the sample remains polarised even to high temperatures, which is consistent with static defect dipoles. Finally, we note that the low growth temperature sample heated in air appear to return to its initial up polarised state after the measurements, as determined by PFM images taken before and after, unlike the samples heat treated in-situ in the growth chamber at lower pressure (180 mTorr) shown in Fig. 5.4. This observation suggests that for full control control of the polarisation, the heating should be carried out under low oxygen conditions, as is also apparent from Ref. [40], and that the Pb-O vacancy dipoles are fixed after they form.

5.10 Conclusion

We have achieved full deterministic control of the intrinsic polarisation state of ferroelectric thin films, independently of the electrostatic boundary conditions. We were able to target the polarization state to be monodomain up, monodomain down, or polydomain, stable ex-situ for at least two years, simply through the use of temperature during film deposition, while maintaining full in-plane epitaxial strain and high surface and crystalline quality. We have shown moreover that this control can be extended beyond the growth stage of the film, and also achieved with a subsequent in-situ annealing. Growth temperature is a particularly easy parameter to access, thus allowing modulation in most of the available growth and deposition systems. Beyond the purely monodomain films, our work offers an additional tuning parameter to create and stabilise extremely small domains with the potential for unusual polarization textures, including nanoscopic bubble domains, vortex and skyrmion-like topologies, opening new perspectives in the fast developing field of domain engineering.

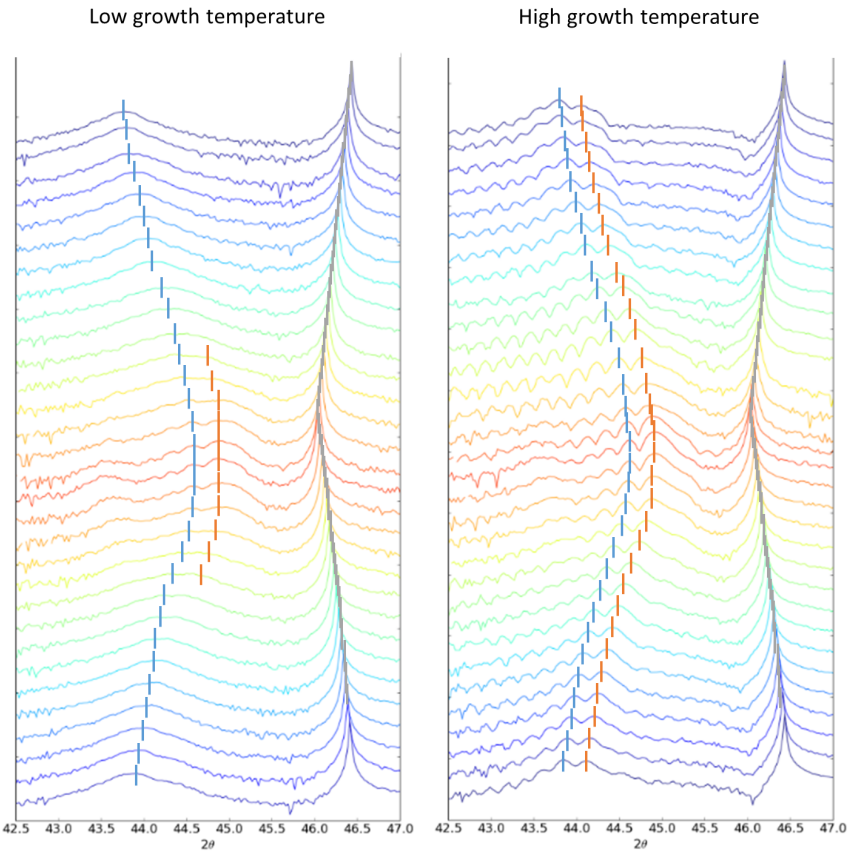

Figure 5.14: Temperature series of diffractograms for a low growth temperature and a high growth temperature sample. Colour indicates temperature of the measurement, and vertical position indicates temporal sequence (first scan on top, last scan at the bottom). Markers for the peaks are a guide to the eye. We can clearly see spectral weight shifting from the high c-axis peak to the low c-axis peak for the high growth temperature sample, and a low c-axis peak appearing for the high growth temperature sample.

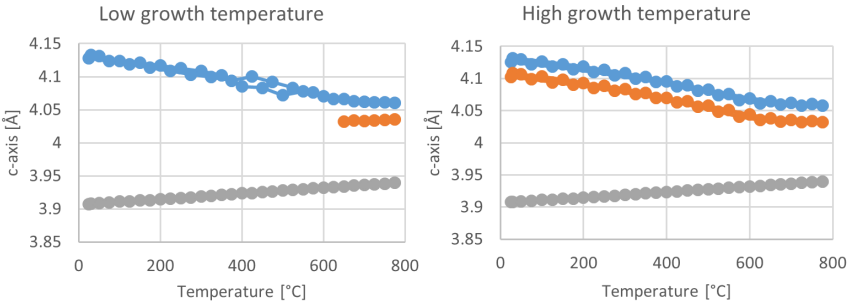

Figure 5.15: (Average) c-axis extracted from the positions of the peaks marked in Fig. 5.14. The upturn above 600°C indicates the ferroelectric to paraelectric phase transition.

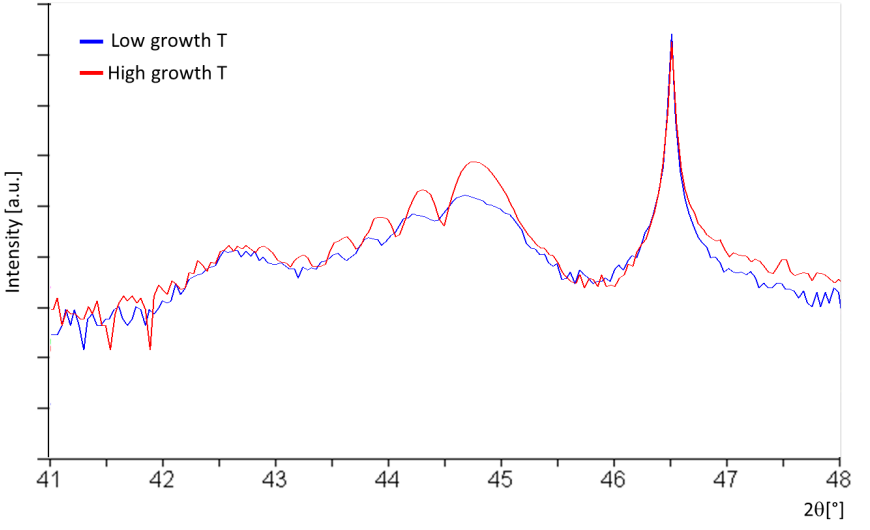

Figure 5.16: Comparison of the highest temperature spectra for both samples shown in Fig. 5.14. At this temperature, both samples show the same features, indicating that both have a region of higher than average polarisation, consistent with a model where localised defect dipoles maintain polarisation in some parts of the sample even above the transition temperature.

CHAPTER 6

Slow Kinetics Intermittent Sputtering

6.1 Introduction

To take advantage of the multitude of functional properties complex oxide offer for miniaturised applications [104–106], cheap and scalable methods are needed for their deposition. More fundamentally, extended defects such as grain boundaries and dislocations, as well as dopants and stoichiometry variations can be to a large extent eliminated or relatively precisely engineered in monocrystaline, epitaxial thin films. This makes them a great system to study the intrinsic properties of these materials. To obtain such high quality thin films, physical vapour deposition techniques are the method of choice. Of the three main such techniques - molecular beam epitaxy, pulsed laser deposition, and radio-frequency (RF) magnetron sputtering - the latter is by far the cheapest to implement, since it requires neither ultra-high vacuum nor expensive laser equipment. RF magnetron sputtering has been very successfully applied for many oxide systems, and in particular ferroelectrics, producing extremely high quality thin films [28, 107, 108] and superlattices [4, 109, 110] with atomically sharp interfaces, and more recently, solid solutions whose properties can be continuously tuned via their stoichiometry [18]. For a more technical oriented introduction to this deposition technique, the reader is referred to Sect. 4.4.

Despite the great success of this technique in producing ultra-thin films and superlattices, growing films thicker than approximately 10 unit cells can be challenging for certain materials. Many different growth parameters

need to be optimised to obtain good quality films, a task which is slowed down by the fact that sputtering usually does not allow for in-situ monitoring of the growth by reflection high energy electron diffraction (RHEED), routinely used during pulsed laser deposition or molecular beam epitaxy. However, once the optimal parameters are determined, they are usually very stable in time, and lead to consistently high quality films. One of the key optimisation parameters is the growth temperature, which can moreover be used to control the functional properties of the thin films via defect gradient engineering (see Chapter 5) or strain relaxation [36, 37]. However, moving this parameter outside the optimal growth window can be detrimental to the crystalline quality of the films, thus limiting its applicability. Here, we present a technique that allows us to increase the temperature range over which the samples present a consistently high crystalline quality, opening the possibility to use temperature as a tuning parameter for the functional properties of the sample. We demonstrate this technique in 50 nm films of lead titanate ($PbTiO_3$), which is a prototypical tetragonal ferroelectric, and which has been grown by sputtering for more than two decades [4, 28, 107–110].

Inspired by the ease with which solid solutions can be grown from two targets [18], and by similar approaches for pulsed laser deposition [111], where the target material is deposited via intermittent pulses alternating with waiting periods of several seconds, we decided to modify our deposition technique to allow more time for the realisation of slow kinetic processes at the surface of the growing film, resulting in Slow Kinetics Intermittent Sputtering (SKIS, see Fig. 6.1). In this technique, the RF gun is turned on for approximately one minute, a quarter of the time needed to deposit a full unit cell. The gun is then switched off completely for approximately 20 seconds, to allow the newly deposited adatoms to relax and optimise their position on the surface, similarly to what is shown by in-situ RHEED in Ref. [111], and the process is repeated until the desired thickness of material is deposited (Fig. 6.2(a)). We found that longer relaxation times did not change the sample characteristics, and shorter relaxation times were hard to obtain with our experimental set up. The results presented in this Chapter also gave rise to the publication Ref. [112].

6.2 Results and discussion

We first applied our SKIS deposition technique to produce bilayers consisting of 50 nm thick ferroelctric $PbTiO_3$ films on top of a lanthanum nickelate ($LaNiO_3$) bottom electrodes, grown on (001)-oriented strontium titanate ($SrTiO_3$) substrates. Detailed growth conditions for all samples in this study can be found in Appendix A. Fig. 6.2(b) shows the AFM surface topographies

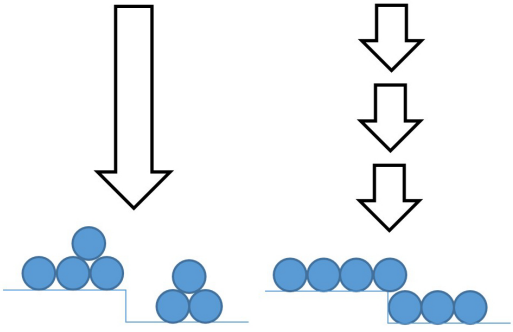

Figure 6.1: Schematic representation of our method: instead of depositing all the material continuously (left), we intermittently sputter and wait, to allow the adatoms to relax and rearrange on the surface (right).

(see Sect. 4.1.1) of four samples in a series grown in continuous mode to optimise the growth temperature, all on the same 2 nm colour scale. We can see that outside the optimal growth range of 540-570°C, where the RMS roughness is less than one unit cell, the surface morphology greatly deteriorates, with holes and pillars appearing. In contrast when SKIS mode is used (Fig. 6.2(c)), while the RMS roughness remains higher for very low growth tempareture, all the samples through the same temperature range show far more homogeneous morphology and remain extremely flat, even for very high growth temperatures. This observation demonstrates that the SKIS technique allows us to grow high quality samples in a broader temperature range than the conventional continuous sputtering deposition approach.

We now focus on two pairs of samples, again all 50 nm thick, grown one immediately after the other, one at each end of the optimal temperature range for surface quality in the continuous mode, and two samples grown at the same temperatures in SKIS mode. The x-ray diffractograms (see Sect. 4.2) around the (002) Bragg peaks for both the sample and the substrate are shown in Fig. 6.3(a) for the two samples grown in continuous mode. We can see that, although the sample grown at 570°C shows some finite size oscillations, these are not very marked, and the sample peaks for both films are quite broad, indicating some loss of coherence and therefore less than optimal crystalline quality. The same measurement for the SKIS-grown samples (Fig. 6.3(b)), on the other hand, show very clear finite size oscillations and sharper peaks, both of which are indicative of higher crystalline quality. The diffractograms of these films even present an additional peak (indicated with a * in Fig. 6.3(b)) between the film and the substrate, in the position where a double diffraction peak is expected when the films are coherent enough to allow double diffraction [83, 100], and which we rarely observe with

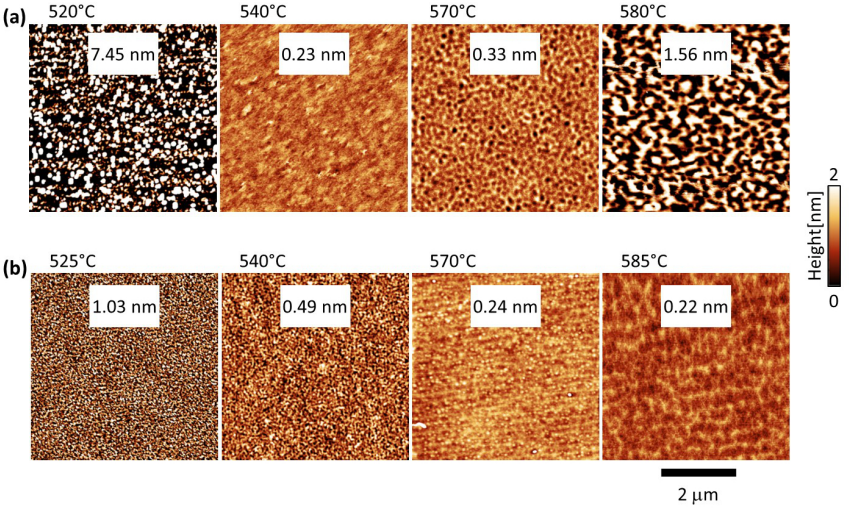

Figure 6.2: Growth temperature range for high surface quality. Surface topographies for a series of samples grown at different temperatures using (a) the continuous mode and (b) the SKIS mode. All images are represented on the same 2 nm colour scale, and the RMS roughness is indicated on each image. We can see that for samples grown continuously outside the range of 540-570°C, the surface roughness increases dramatically, whereas the SKIS-grown samples are much more homogeneous over the entire temperature range investigated, with sub-unit-cell roughnesses up to the highest temperatures.

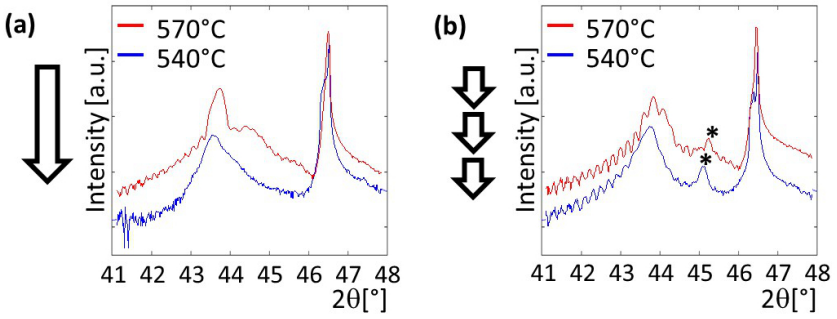

Figure 6.3: Comparison of the x-ray diffractograms around the (002) reflection of the film and the substrate of samples grown at two different growth temperatures in the continuous mode (a) and in the SKIS mode (b) in immediate succession. For both growth temperatures, SKIS-grown samples show significantly higher crystalline quality, as evidenced by the more pronounced finite size oscillations and the appearance of a double diffraction peak (indicated with a *) signalling high coherence [83, 85, 100].

the continuous sputtering approach. This comparison further shows that, where the growth temperature has a strong impact on the quality of the thin films for continuous growth, SKIS mode allows us to grow high crystalline quality films over a broad temperature range, in addition to producing a more coherent structure at all growth temperatures. In light of the importance of the growth temperature to tune the Pb-O dipolar vacancies, demonstrated in Chapter 5, the ability to grow high quality samples over a larger temperature range is crucial for device applications.

To test how well this approach works for other systems, we applied the SKIS deposition technique to a range of materials with different crystal symmetries. All the samples were grown on the same substrate as the $PbTiO_3$ thin films, (001)-oriented $SrTiO_3$. The materials we selected were homoepitaxial cubic $SrTiO_3$, rhombohedral $BiFeO_3$ with an $LaNiO_3$ bottom electrode, and orthorhombic $LaFeO_3$. In each case, two samples were grown in immediate succession, one in continuous mode, one in SKIS mode. The growth parameters used were the ones that had been previously optimised using continuous deposition for each of the materials. Comparison between the x-ray diffractograms around the (002) reflection are shown in Fig. 6.4. For $SrTiO_3$ (Fig. 6.4(a)), the shape of the peaks for both samples corresponds to a film about 20 nm thick, with a c-axis of 3.911 Å, slightly higher than the expected 3.905 Å, which is also the lattice parameter of the substrate, thus showing a slight off-stoichiometry of both films. For $BiFeO_3$ and $LaFeO_3$ (Fig. 6.4(b)-(c)), both samples show very well defined peaks and finite size oscillations, indicating very high crystalline quality. All three materials show virtually identical diffraction patterns for both the continuous and the SKIS grown samples. Note that the $BiFeO_3$ and $LaFeO_3$ were grown in a different

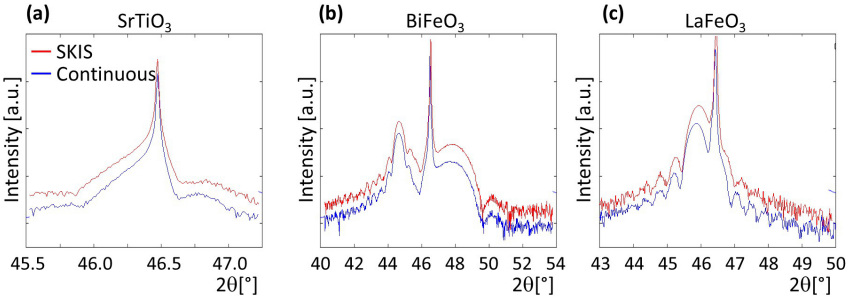

Figure 6.4: Comparison of the diffractograms around the (002) reflection of the film and the substrate for materials with different symmetries than tetragonal $PbTiO_3$: (a) cubic $SrTiO_3$ (homoepitaxial) (b) Rhombohedral $BiFeO_3$ on $SrTiO_3$, with a $LaNiO_3$ back-electrode and (c) orthorhombic $LaFeO_3$ on $SrTiO_3$. For all these materials, since the growth conditions were already highly optimised, the change in deposition mode had no visible impact on the (very high) crystalline quality of the samples.

growth chamber from the $PbTiO_3$ and $SrTiO_3$, which excludes a system specific effect. These observations indicate that when growth conditions are fully optimised, SKIS works just as well as continuous growth, i.e. the waiting time does not destroy order that would otherwise be present.

6.3 Conclusion

To summarise, we have shown a very easy-to-implement adaptation that has allowed us to significantly increase the growth window that produces high quality $PbTiO_3$ thin films using RF magnetron sputtering. We have also shown that although this approach does not have any additional benefits for highly optimised growth conditions, it also does not seem to disturb the order already present in films grown under these conditions. We hope our observations will inspire other groups to try this approach on materials they might have a hard time optimising the growth conditions for, and that this technique will expand the range of materials available to RF magnetron sputtered thin films. Furthermore, the ability to change the growth temperature without deteriorating the film quality will lead to more possibilities to tailor functional properties to one's needs. Industrial application will undoubtedly greatly benefit from a wider pool of available materials and a larger range of available tuning parameters in a cost effective and scalable deposition technique.

CHAPTER 7

Non-Ising domain walls in lead titanate thin films

Non-Ising domain walls in nominally uniaxial ferroelectrics are currently the subject of intense research efforts, see Sect. 2.2.4. Most recently, the prediction of ferroelectric skyrmions in $PbTiO_3$ thin films [7], and their subsequent experimental discovery in $PbTiO_3/SrTiO_3$ superlattices [8] has fascinated the community. Unlike in magnetic materials, where skyrmions are typically considered two dimensional, and can be classified according to the type of rotation of the magnetisation on a line passing through the centre of the skyrmion (Néel vs Bloch), the observed ferroelectric skyrmions were three dimensional objects, with the polarisation arranged in a Néel-type fashion at the top, a Bloch-like fashion in the centre, and a Néel-type fashion pointing in the opposite direction at the bottom of the structure, leading to flux closure around the wall. The question of the type of domain walls present in $PbTiO_3$ thin films has long been open to debate: whereas some theoretical calculations predict Néel type walls [6, 113], just as in $Pb(Zr_{0.2}Ti_{0.8})O_3$ [69], other calculation predicted Bloch walls at low temperature [66], a necessary element of the chiral structures predicted by Gonçalves *et al.* [7], where the in-plane component along the wall forms a closed loop around a domain. We therefore set out to measure the type of domain walls present in $PbTiO_3$ thin films, without the extra complications of the superlattice structure, and 5 to 10 times thicker than a single layer in the superlattice.

To achieve this, two samples were measured using second harmonic generation (SHG, see Sect. 4.3) by S. Cherifi-Hertel: a monodomain up sample and a polydomain sample, to try and compare written domains with intrinsic ones. The results of these measurements and our subsequent

analysis are presented in the rest of this chapter.

7.1 Monodomain samples: written domains

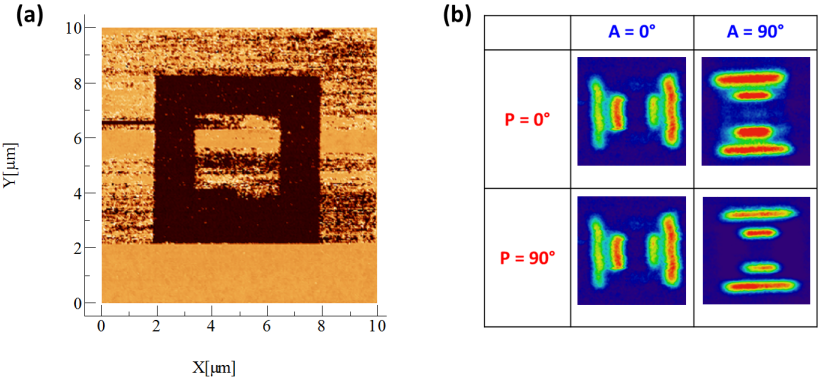

Figure 7.1: SHG polarimetry on written domains. (a) PFM image of the written domain structure that was analysed, a square-in-square pattern. (b) Second harmonic generation signal for the domain structure shown in (a) for different polariser (P) and analyser (A) angles. This signal is consistent with walls with a Néel component and no Bloch component.

To investigate the nature of written domain walls in PTO, we first wrote a domain pattern large enough to be resolved by the SHG setup. A PFM image of the written pattern is shown in Fig. 7.1(a): a 3×3 µm^2 square of up polarisation, inside a 6×6 µm^2 square of down polarisation, against the up polarised background. We then performed SHG polarimetry. As explained in Sect. 4.3 and in Ref. [69], for polariser angles of 0° and 90°, the SHG light will be fully polarised along the in-plane polarisation at the wall. Fig. 7.1(b) shows the result of this analysis: the domain walls are clearly visible in the SHG image when the analyser is perpendicular to them. This shows that, for written walls at room temperature, domain walls in $PbTiO_3$ thin films are Néel-type with no Bloch component. We were not able to perform the same measurements at lower temperature, so it is possible that there is a phase transition inside the walls from Néel- to Bloch-type below room temperature, as first-principles calculations suggest that the walls should have a Bloch character at low temperature [66].

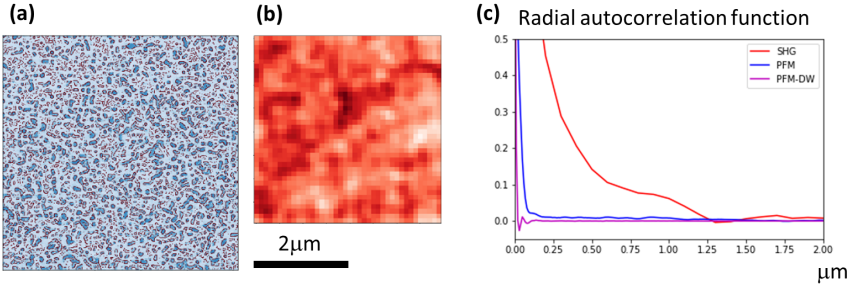

Figure 7.2: (a) PFM image of the domains (blue) and the domain walls (red) detected using the Canny algorithm. (b) SHG image of the same sample on the same lateral length-scale. (c) Radially averaged autocorrelation function for the images presented in (a)(domains and domain walls) and (b). The first maximum indicates the pseudo-periodicity. We can see that the SHG image shows some contrast on a scale that does not correspond to the size of the domains.

7.2 Polydomain samples: intrinsic domains

The intrinsic domains in our films are much smaller than the resolution of SHG. Indeed, PFM (Fig. 7.2(a)) shows that they are on the order of 50 nm across, well below the diffraction limit for the wavelength used, which is about 300 nm. Nonetheless, SHG images taken on a polydomain film, for example Fig. 7.2(b) taken over a region of interest of 4×4 µm^2, still show some regions of brighter and darker contrast. However, when trying to visually compare this contrast to a PFM image of the same sample (Fig. 7.2(a)), we see that it appears on a much longer length-scale. Nonetheless, we do observe that there are variations in the density of the nanoscale domains, and we wondered if these may be correlated with the variations of contrast observed in SHG.

Precise visual comparison of these two images is challenging, therefore we turn to a more quantitative statistical tool: radially averaged autocorrelation, which measures the total correlation between an image and a copy of that image shifted by a certain distance in any direction. This allows us to extract a characteristic feature size from each image, given by the position of the first minimum in the radially averaged autocorrelation curve, as well as a pseudo-period, given by the position of the first maximum on the curve. The results are shown in Fig. 7.2(c): the SHG image shows no clear characteristic feature size, possibly due to a too big heterogeneity of the features, however it seems to have a pseudo-period of approximately 1 µm. PFM on the other hand shows a pseudo-period of about 100 nm, which corresponds to the domain structure, and no further marked peaks which could indicate a periodicity in the domain density variations. The results for the domain walls, extracted using a Canny edge detection algorithm, is even more extreme: beyond the

scale of a domain, the correlation is constantly very close to 0.

To access the variations in local density of domains and domain walls, we explicitly blurred out the microstructure by convoluting our PFM images with a Gaussian kernel with a standard deviation of $\sigma = 100\,\text{nm}$, larger than any individual domain, and a size of at least 3σ in all directions to ensure a smooth result. This is equivalent to replacing each point in the image with a Gaussian weighted average of all of the pixels in its neighbourhood. The resulting image is shown in Fig. 7.3(a) for the domains and (b) for the domain walls. The variations in domain and domain wall density we inferred from visual inspection are clearly revealed. If we now again extract the pseudo-period of this superstructure using the radially averaged autocorrelation, we can see that it is the same as the pseudo-period of the intensity variations in the SHG image Fig. 7.3(c).

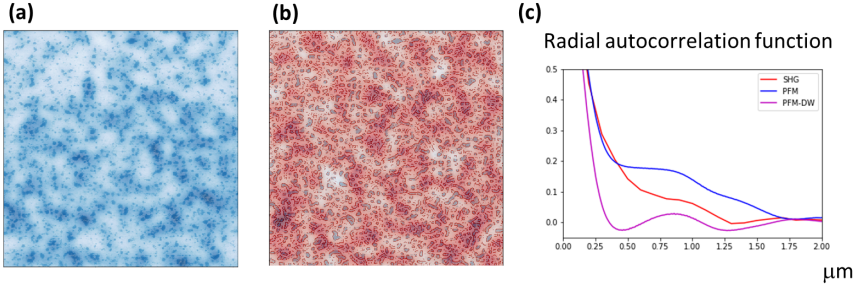

Figure 7.3: Blurring and the radially averaged autocorrelation function. (a) PFM domain and (b) domain wall image blurred using a Gaussian kernel with a standard deviation of 100 nm, superimposed on the original image. (c) Radially averaged autocorrelation function for the blurred images and the SHG image presented in Fig. 7.2(b). The blurring process reveals the superstructure, which has a similar pseudo-periodicity to the SHG image.

To further investigate a possible origin of these density variations, we turned to simulations using the Ising model with an added potential containing a specific length-scale. The parameters of the unperturbed model were chosen such that up and down polarisation (in equal proportion) were randomly distributed (see, for example, Fig. 7.4(c)). A random potential was then generated by first choosing a radius (in pixel), then filling the simulation grid with circles of that radius (limiting the overlap to 25% of each circle's area), where each circle had a slight positive or negative potential energy associated with it (see Fig. 7.4(a)). The circles were then blurred using a Gaussian filter to mimic a random disorder pinning potential with a certain correlation length ξ, beyond which the effect of the disorder decays (see Fig. 7.4(b)). The resulting potential was then added to the Ising Hamiltonian, and the simulation allowed to relax (see Fig. 7.4(d)). For each radius, a

hundred potential configurations were generated and run. We then applied the same process to the resulting domain structures as we applied to the PFM images, before averaging over the different potential configurations for each radius. By blurring out the microstructure to reveal the superstructure, and then using the radially averaged autocorrelation function to extract the pseudo-period and the typical feature size, we see that the feature size, given by the first minimum in the radially averaged autocorrelation function, exactly matches the diameter of the circles that were initially generated (see Fig. 7.5). This indicates that the length-scale observed in SHG and in the superstructure of the domain distribution of our sample may provide information about the typical correlation lengths of the disorder potential, and thus about the dominant defects in the film and their distribution.

The work on these intrinsic domains is still ongoing. Theoretical analysis is needed to identify the type of defect that could be responsible for the appearance of such a length scale. Polarimetry analysis of the SHG signal of the superstructure might be able to give us information on the nature of the domain walls of individual domains, if the polarisation in the walls lies in a consistent direction and does not average out at the edges of the clusters. Circularly polarised SHG microscopy could also help reveal the chirality of the intrinsic domains, if it is there. Finally, temperature dependent PFM and conductive-AFM measurements might pick up a change in domain pattern or conduction at the domain wall, which could indicate a transition from Néel-type to Bloch-type walls. Further research along one or several of these avenues is bound to reveal some interesting physics in these intrinsic domain walls.

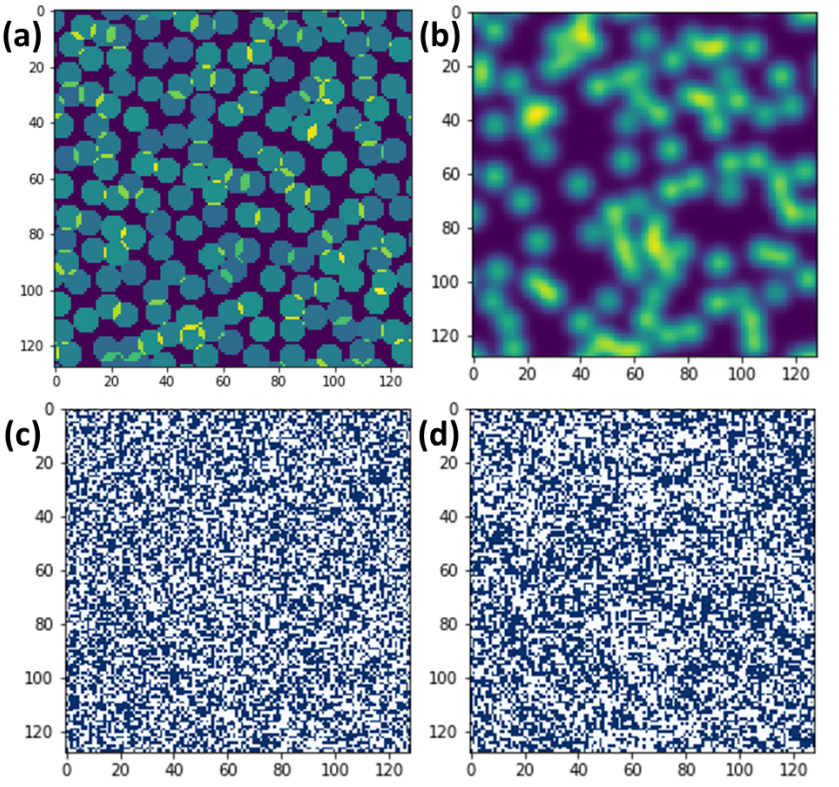

Figure 7.4: The Ising model with an added potential. (a) Example of initial circle distribution for a radius of 5. (b) The potential generated from the configuration in (a). Yellow represents high values and blue low values. (c) Initial domain configuration: the blue and white domains are randomly distributed. (d) Relaxed domain structure after adding the potential shown in (b) to the Ising Hamiltonian. Notice that there are more white domains in the regions of high potential, and more blue domains in the regions of low potential.

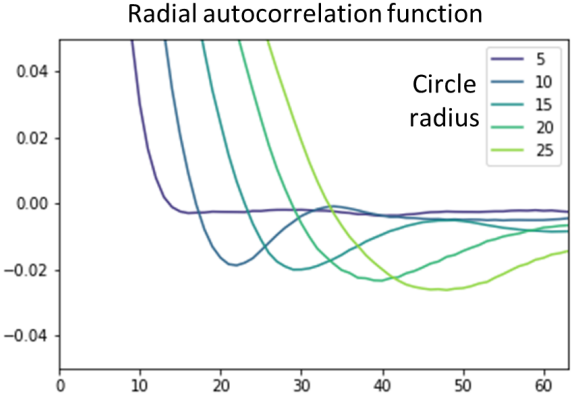

Figure 7.5: The radially averaged autocorrelation function of the blurred relaxed domain structure for each initial circle radius, averaged over one hundred realisations of the potential for each radius. We can see that the typical feature size in the superstructure, given by the first minimum to the radially averaged autocorrelation function, corresponds exactly to the diameter of the initial circles.

CHAPTER 8

Conclusions and perspectives

Ferroelectric materials are of great fundamental and technological interest. Modern thin film fabrication techniques have allowed a thorough exploration of their properties, many of which are modified by the presence of domains. Many studies have demonstrated the ability to control the polarisation state of ferroelectric samples, however, this was systematically either accompanied by other changes to the sample, such as a change to the electrostatic boundary conditions for example, or by extra processing steps. In this thesis, we set out to fabricate series of $PbTiO_3$ thin films, which only differ by their polarisation state, and whose polarisation states are intrinsic and stable.

We showed that, independently of the electrostatic boundary conditions, changing the deposition temperature of our samples allowed us to fully control their intrinsic polarisation state, as demonstrated by piezoresponse force microscopy, both in imaging and spectroscopic mode. Furthermore, we showed that a similar effect could be achieved by heating the samples in the process gas after the growth. Rutherford backscattering spectroscopy showed significant variations in lead stoichiometry, both between the samples grown at different growth temperatures, but also, for lead deficient samples, between the regions close to their surface and the regions in their interior. This lead to the microscopic model of a gradient of lead-oxygen defect dipoles, aligned by the internal field present during growth, which stabilised the corresponding polarisation orientation. This model was supported by the observation of a strain gradient across the films by x-ray diffraction, which was linked using Ginzburg-Landau-Devonshire theory to a variation in polarisation throughout the film, commensurate with the contribution to

the polarisation expected from the defect dipoles. Furthermore, this model was also able to explain our observations on films of varying thickness, as well as x-ray diffractograms of samples heated in ambient conditions.

We then presented a technique that allowed us to grow very high quality thin films over a wide range of growth temperatures. By periodically interrupting the deposition by radio-frequency magnetron sputtering, we achieved Slow Kinetics Intermittent Sputtering (SKIS) by leaving more time for the position of the newly deposited adatoms to equilibrate. This lead to a drastic increase of the "growth window" for $PbTiO_3$, the range of deposition temperatures over which the quality of our films is high, making it large enough to obtain samples in any polarisation state. This was shown by atomic force microscopy surface imaging, as well as x-ray diffraction, two standard techniques to asses the quality of thin films. Moreover, for growth conditions optimised for continuous growth, cubic $SrTiO_3$, rhombohedral $BiFeO_3$, and orthorhombic $LaFeO_3$ all showed quality as high for the intermittent deposition as for the continuous one, proving the applicability of SKIS to a wide range of materials.

Finally, we presented some of our ongoing work on one of the possible applications of films which only differ by their polarisation state. The internal structure of domain walls in $PbTiO_3$ is a subject of very active research, and we used second harmonic generation microscopy to probe it both in written domain walls on a monodomain sample, and in intrinsic domain walls on a polydomain sample. The written walls show a clear Néel character at room temperature, unlike what was recently reported for the skyrmion-like intrinsic domains in $PbTiO_3/SrTiO_3$ superlattices [8]. The intrinsic domains, on the other hand, were too small to be resolved by the microscope, but the images still showed a pseudo-periodic contrast. By analysing our piezoresponse force microscopy images of the same sample using the radially averaged autocorrelation function, we could show, after intentionally blurring out the domain microstructure, that this contrast was likely due to a superstructure in the domain distribution. By modifying a simple Ising model to include a defect potential with a characteristic lengthscale, we could show that this superstructure could be caused by such a potential. Additional analysis and measurements are needed to determine a possible type of defect acting at the observed lengthscale, as well as to get a definitive answer on the internal structure of the intrinsic domain walls.

Another example of a future project making good use of the possibility to have samples which differ only by their polarisation state is the analysis of the interaction between polarisation and surface water. Indeed, this highly polar molecule has been shown to be strongly influenced by the different bound charge resulting from different polarisation orientations, but also by surface morphology, and writing history [114, 115]. Having a series of three samples, one up polarised, one down polarised, and one polydomain,

with no other intrinsic differences, would allow us to study the effects on condensation and icing linked only to the intrinsic polarisation, and compare them to the effects of written domains. Any study where there might be differences between the behaviour of intrinsic domains and written domains would benefit from such a series of samples.

APPENDIX A

Growth conditions

The following table lists all the growth conditions of the materials used in this thesis. Unless specified in the text, all samples were grown on TiO_2 terminated, (001)-oriented, undoped $SrTiO_3$. The meaning of all parameters is explained in Sect. 4.4. The target column indicates any off-stoichiometry of the used targets. The split in the table indicates two different growth chambers.

Material	RF-power(W)	Pressure (mtorr)	O_2:Ar	Growth temperature (°C)	Target
$PbTiO_3$	60	180	20:29	520-590	10% Pb excess
$SrRuO_3$	80	100	3:60	645	
$LaNiO_3$	50	180	10:35	same as $PbTiO_3$ thin film	
$SrTiO_3$	60	180	20:29	540	
$BiFeO_3$	40	100	25:75	650	10% Bi excess
$LaNiO_3$	50	100	30:70	550	
$LaFeO_3$	50	100	25:75	650	

Remerciements

L'écriture d'une thèse est aussi, comme souvent en sciences, un effort collectif. Je voudrais prendre ici un moment pour remercier sincèrement tous les collaborateurs, collègues, et amis qui m'ont accompagnés tout au long de cette aventure. Je n'aurais pas pu y arriver sans leur soutien, leur expertise et leurs conseils avisés.

Je tiens tout d'abord à remercier chaleureusement Patrycja Paruch d'avoir accepté d'être ma directrice de thèse. Sa confiance et son expérience m'ont permis de suivre la voie indiquée par les résultats expérimentaux jusqu'au bout, sans perdre mon chemin. Elle m'a offert de nombreuses opportunités d'aller à la rencontre de la communauté scientifique internationale, qui ont été l'occasion de rencontres et d'échanges passionnants. Cela m'a aidé à découvrir ce qu'est vraiment la science, et j'en suis très reconnaissant.

Après avoir dirigé mon projet de Master, Jean-Marc Triscone a accepté d'être mon co-directeur de thèse. Il a su me fournir un environnement optimal à sa réalisation. Ses conseils toujours avisés et sa vision d'ensemble m'ont bien souvent permis de me sortir d'une impasse. Un grand merci pour sa confiance et son énergie positive.

Toute ma gratitude va également à Céline Lichtensteiger, qui a suivi mon travail depuis mon projet de Master. C'est elle qui m'a appris tout ce que je devais savoir sur la croissance et la caractérisation de couches minces ferroélectriques. Elle a toujours pris le temps de discuter de mes résultats quand j'étais coincé, de relire mes papiers et les chapitres de cette thèse, et de faire des suggestions avisées sur mes figures et mes présentations.

Je souhaite aussi vivement remercier les membres de mon jury, Radowan Černý, Morgan Trassin, et Jirka Hlinka, pour avoir pris le temps de lire mon manuscrit, et pour leurs questions stimulantes lors de la soutenance.

Tout mes collaborateurs externes m'ont fait profiter de leur expertise. Les données qu'ils ont pu me fournir étaient autant de pièces de puzzle que nous avons assemblées ensembles. Pour cela, je les remercie.

Remerciements

J'ai eu le plaisir de faire partie pendant ma thèse de non pas un mais de deux superbes groupes de recherche, les groupes Paruch et Triscone. La culture de l'ouverture et de la bienveillance qu'ils pratiquent, ainsi que la qualité du support administratif et technique, ont fait de cette expérience un réel plaisir. Je voudrais ici remercier tous leurs membres présents et passés, et tout particulièrement Stéphanie Fernandez-Peña et Iaroslav Gaponenko, qui m'ont beaucoup appris sur les techniques que j'ai employées au quotidien.

Marc Philippi, Guillaume Rapin, et Philippe Tückmantel ont partagé pour ainsi dire tout mes repas de midi depuis le début de notre Bachelor, il y a dix ans. Leur bonne humeur et leur fidélité me rendent fier de pouvoir les compter parmi mes amis. Merci pour votre soutien au quotidien, et, au sens étymologique du terme, votre compagnie.

Un grand merci également à famille, qui m'a toujours soutenu et guidé, et qui a fait de moi ce que je suis aujourd'hui. Votre fierté m'honore.

Mes amis ont été pour moi une deuxième famille depuis l'adolescence. Un grand merci à Robin, Elliott, Jean-Pierre, Dimitri, Aloys, Nadine, Noémi, Anouck, et les autres membres du Groupe de Nous, pour votre bonne humeur, pour l'intérêt que vous avez porté à mon sujet d'étude pas toujours très accessible, et pour votre soutien sans faille.

Enfin, j'ai une pensée toute particulière pour Mireille, qui m'a soutenu (et supporté) pendant toutes ces années de thèse. Elle a partagé mes moments de joie, m'a écouté me plaindre, et pardonné mes moments de stress. Merci d'être là pour moi en toutes circonstances.

Bibliography

[1] J. Valasek, "Piezo-electric and allied phenomena in rochelle salt", Phys. Rev. **17**, 475–481 (1921).

[2] M. E. Lines and A. M. Glass, *Principles and applications of ferroelectrics and ralated materials* (Oxford University Press, 1977).

[3] J. F. Scott, *Ferroelectric memories*, Vol. 3 (Springer, 2000).

[4] P. Zubko et al., "Negative capacitance in multidomain ferroelectric superlattices", Nature **534**, 524–528 (2016).

[5] J. Seidel et al., "Conduction at domain walls in oxide multiferroics", Nature Mater **8**, 229–234 (2009).

[6] D. Lee et al., "Mixed Bloch-Néel-Ising character of 180° ferroelectric domain walls", Phys. Rev. B **80**, 060102 (2009).

[7] M. A. P. Gonçalves et al., "Theoretical guidelines to create and tune electric skyrmion bubbles", Science Advances **5**, eaau7023 (2019).

[8] S. Das et al., "Observation of room-temperature polar skyrmions", Nature **568**, 368–372 (2019).

[9] A. von Hippel et al., "High dielectric constant ceramics", Ind. Eng. Chem. **38**, 1097–1109 (1946).

[10] B. Wul, "Barium titanate: a new ferro-electric", Nature **157**, 808–808 (1946).

[11] U. V. Waghmare and K. M. Rabe, "Ab initio statistical mechanics of the ferroelectric phase transition in $PbTiO_3$", Phys. Rev. B **55**, 6161–6173 (1997).

[12] P. Ghosez et al., "Lattice dynamics of $BaTiO_3$, $PbTiO_3$, and $PbZrO_3$: A comparative first-principles study", Phys. Rev. B **60**, 836–843 (1999).

[13] P. Ghosez and K. M. Rabe, "Microscopic model of ferroelectricity in stress-free $PbTiO_3$ ultrathin films", Appl. Phys. Lett. **76**, 2767–2769 (2000).

[14] M. V. R. Murty et al., "In situ x-ray scattering study of $PbTiO_3$ chemical-vapor deposition", Appl. Phys. Lett. **80**, 1809–1811 (2002).

[15] M. Dawber et al., "Tailoring the properties of artificially layered ferroelectric superlattices", Advanced Materials **19**, 4153–4159 (2007).

[16] P. Zubko et al., "X-ray diffraction studies of 180° ferroelectric domains in $PbTiO_3/SrTiO_3$ superlattices under an applied electric field", Phys. Rev. Lett. **104**, 187601 (2010).

[17] C. Lichtensteiger et al., "Tuning of the depolarization field and nanodomain structure in ferroelectric thin films", Nano Letters **14**, 4205–4211 (2014).

[18] S. Fernandez-Peña et al., "Ferroelectric domains in epitaxial $Pb_xSr_{1-x}TiO_3$ thin films investigated using X-ray diffraction and piezoresponse force microscopy", APL Materials **4**, 086105 (2016).

[19] A. K. Yadav et al., "Observation of polar vortices in oxide superlattices", Nature **530**, 198–201 (2016).

[20] W. Cochran, "Crystal stability and the theory of ferroelectricity", Advances in Physics **9**, 387–423 (1960).

[21] R. E. Cohen, "Origin of ferroelectricity in perovskite oxides", Nature **358**, 136–138 (1992).

[22] R. D. King-Smith and D. Vanderbilt, "Theory of polarization of crystalline solids", Phys. Rev. B **47**, 1651–1654 (1993).

[23] R. D. King-Smith and D. Vanderbilt, "First-principles investigation of ferroelectricity in perovskite compounds", Phys. Rev. B **49**, 5828–5844 (1994).

[24] R. Resta, "Macroscopic polarization in crystalline dielectrics: the geometric phase approach", Rev. Mod. Phys. **66**, 899–915 (1994).

[25] R. Resta, "Quantum-mechanical position operator in extended systems", Phys. Rev. Lett. **80**, 1800–1803 (1998).

[26] N. A. Spaldin, "A beginner's guide to the modern theory of polarization", Journal of Solid State Chemistry **195**, 2–10 (2012).

[27] W. Zhong, R. D. King-Smith, and D. Vanderbilt, "Giant LO-TO splittings in perovskite ferroelectrics", Phys. Rev. Lett. **72**, 3618–3621 (1994).

[28] C. Lichtensteiger et al., "Built-in voltage in thin ferroelectric $PbTiO_3$ films: the effect of electrostatic boundary conditions", New Journal of Physics **18**, 043030 (2016).

[29] B. Meyer and D. Vanderbilt, "Ab initio study of ferroelectric domain walls in $PbTiO_3$", Phys. Rev. B **65**, 104111 (2002).

[30] C. Kittel, "Theory of the structure of ferromagnetic domains in films and small particles", Phys. Rev. **70**, 965–971 (1946).

[31] L. Landau and E. Lifshitz, "On the theory of the dispersion of magnetic permeability in ferromagnetic bodies", Phys. Z. Sowjetunion **8**, 153 (1935).

[32] G. Catalan et al., "Wall thickness dependence of the scaling law for ferroic stripe domains", Journal of Physics: Condensed Matter **19**, 022201 (2007).

[33] G. Liu et al., "Positive effect of an internal depolarization field in ultrathin epitaxial ferroelectric films", Advanced Electronic Materials **2**, 1500288 (2016).

[34] P. V. Yudin and A. K. Tagantsev, "Fundamentals of flexoelectricity in solids", Nanotechnology **24**, 432001 (2013).

[35] P. Zubko, G. Catalan, and A. K. Tagantsev, "Flexoelectric effect in solids", Annual Review of Materials Research **43**, 387–421 (2013).

[36] B. C. Jeon et al., "Flexoelectric effect in the reversal of self-polarization and associated changes in the electronic functional properties of $BiFeO_3$ thin films", Advanced Materials **25**, 5643–5649 (2013).

[37] D. Lee et al., "Flexoelectric control of defect formation in ferroelectric epitaxial thin films", Advanced Materials **26**, 5005–5011 (2014).

[38] R. V. Wang et al., "Reversible chemical switching of a ferroelectric film", Phys. Rev. Lett. **102**, 047601 (2009).

[39] M. J. Highland et al., "Polarization switching without domain formation at the intrinsic coercive field in ultrathin ferroelectric $PbTiO_3$", Phys. Rev. Lett. **105**, 167601 (2010).

[40] M. J. Highland et al., "Equilibrium polarization of ultrathin $PbTiO_3$ with surface compensation controlled by oxygen partial pressure", Phys. Rev. Lett. **107**, 187602 (2011).

[41] Q. M. Zhang et al., "Direct evaluation of domain wall and intrinsic contributions to the dielectric and piezoelectric response and their temperature dependence on lead zirconate titanate ceramics", Journal of Applied Physics **75**, 454–459 (1994).

[42] D. V. Taylor and D. Damjanovic, "Evidence of domain wall contribution to the dielectric permittivity in PZT thin films at sub-switching fields", Journal of Applied Physics **82**, 1973–1975 (1997).

[43] Y. L. Wang et al., "Giant domain wall contribution to the dielectric susceptibility in $BaTiO_3$ single crystals", Appl. Phys. Lett. **91**, 062905 (2007).

[44] L. Jin, V. Porokhonskyy, and D. Damjanovic, "Domain wall contributions in $Pb(Zr,Ti)O_3$ ceramics at morphotropic phase boundary: A study of dielectric dispersion", Appl. Phys. Lett. **96**, 242902 (2010).

[45] A. Kopal et al., "Displacements of 180° domain walls in electroded ferroelectric single crystals: The effect of surface layers on restoring force", Ferroelectrics **223**, 127–134 (1999).

[46] Q. Zhang, R. Herchig, and I. Ponomareva, "Nanodynamics of ferroelectric ultrathin films", Phys. Rev. Lett. **107**, 177601 (2011).

[47] A. M. Bratkovsky and A. P. Levanyuk, "Very large dielectric response of thin ferroelectric films with the dead layers", Phys. Rev. B **63**, 132103 (2001).

[48] I. Luk'yanchuk, A. Sené, and V. M. Vinokur, "Electrodynamics of ferroelectric films with negative capacitance", Phys. Rev. B **98**, 024107 (2018).

[49] H. Yokota et al., "Direct evidence of polar nature of ferroelastic twin boundaries in $CaTiO_3$ obtained by second harmonic generation microscope", Phys. Rev. B **89**, 144109 (2014).

[50] M. Daraktchiev, G. Catalan, and J. F. Scott, "Landau theory of domain wall magnetoelectricity", Phys. Rev. B **81**, 224118 (2010).

[51] S. Y. Yang et al., "Above-bandgap voltages from ferroelectric photovoltaic devices", Nature Nanotech **5**, 143–147 (2010).

[52] S. Farokhipoor and B. Noheda, "Conduction through 71° domain walls in $BiFeO_3$ thin films", Phys. Rev. Lett. **107**, 127601 (2011).

[53] J. Guyonnet et al., "Conduction at domain walls in insulating $Pb(Zr_{0.2}Ti_{0.8})O_3$ thin films", Advanced Materials **23**, 5377–5382 (2011).

[54] T. Sluka et al., "Free-electron gas at charged domain walls in insulating $BaTiO_3$", Nature Communications **4**, 1808 (2013).

[55] D. Meier et al., "Anisotropic conductance at improper ferroelectric domain walls", Nature Mater **11**, 284–288 (2012).

[56] M. Schröder et al., "Conducting domain walls in lithium niobate single crystals", Advanced Functional Materials **22**, 3936–3944 (2012).

[57] G. Catalan et al., "Domain wall nanoelectronics", Rev. Mod. Phys. **84**, 119–156 (2012).

[58] D. Meier, "Functional domain walls in multiferroics", J. Phys.: Condens. Matter **27**, 463003 (2015).

[59] J. R. Whyte et al., "Ferroelectric domain wall injection", Advanced Materials **26**, 293–298 (2014).

[60] L. J. McGilly et al., "Controlling domain wall motion in ferroelectric thin films", Nature Nanotechnology **10**, 145–150 (2015).

[61] P. Sharma et al., "Nonvolatile ferroelectric domain wall memory", Science Advances **3**, e1700512 (2017).

[62] P. Marton, I. Rychetsky, and J. Hlinka, "Domain walls of ferroelectric $BaTiO_3$ within the Ginzburg-Landau-Devonshire phenomenological model", Phys. Rev. B **81**, 144125 (2010).

[63] V. Stepkova, P. Marton, and J. Hlinka, "Stress-induced phase transition in ferroelectric domain walls of $BaTiO_3$", J. Phys.: Condens. Matter **24**, 212201 (2012).

[64] P. Marton, V. Stepkova, and J. Hlinka, "Divergence of dielectric permittivity near phase transition within ferroelectric domain boundaries", Phase Transitions **86**, 103–108 (2013).

[65] Y.-J. Wang, Y.-L. Zhu, and X.-L. Ma, "Chiral phase transition at 180° domain walls in ferroelectric $PbTiO_3$ driven by epitaxial compressive strains", Journal of Applied Physics **122**, 134104 (2017).

[66] J. C. Wojdeł and J. Íñiguez, "Ferroelectric transitions at ferroelectric domain walls found from first principles", Phys. Rev. Lett. **112**, 247603 (2014).

[67] E. A. Eliseev et al., "Structural phase transitions and electronic phenomena at 180-degree domain walls in rhombohedral $BaTiO_3$", Phys. Rev. B **87**, 054111 (2013).

[68] G. D. Luca et al., "Domain wall architecture in tetragonal ferroelectric thin films", Advanced Materials **29**, 1605145 (2017).

[69] S. Cherifi-Hertel et al., "Non-Ising and chiral ferroelectric domain walls revealed by nonlinear optical microscopy", Nature Communications **8**, 15768 (2017).

[70] V. A. Stoica et al., "Optical creation of a supercrystal with three-dimensional nanoscale periodicity", Nature Materials **18**, 377–383 (2019).

[71] M. Hadjimichael, "Ferroelectric domains in lead titanate heterostructures", PhD thesis (University College London, 2019).

[72] L. Landau, "Theroy of phase transformations", Phys. Z. Sowjetunion **11**, 26 (1937).

[73] L. Landau and E. Lifshitz, *Statistical physics (course of theoretical physics, volume 5)* (Pergamon Press, Oxford, 1959).

[74] V. Ginzburg and L. Landau, "On the theory of superconductivity", Zh. Eksp. Teor. Fiz. **20**, 1064–1082 (1950).

[75] A. F. Devonshire, "XCVI. Theory of barium titanate", The London, Edinburgh, and Dublin Philosophical Magazine and Journal of Science **40**, 1040–1063 (1949).

[76] A. F. Devonshire, "CIX. Theory of barium titanate—Part II", The London, Edinburgh, and Dublin Philosophical Magazine and Journal of Science **42**, 1065–1079 (1951).

[77] A. F. Devonshire, "Theory of ferroelectrics", Advances in Physics **3**, 85–130 (1954).

[78] G. Binnig et al., "Tunneling through a controllable vacuum gap", Appl. Phys. Lett. **40**, 178–180 (1982).

[79] A. Gruverman, O. Auciello, and H. Tokumoto, "Scanning force microscopy for the study of domain structure in ferroelectric thin films", Journal of Vacuum Science & Technology B: Microelectronics and Nanometer Structures Processing, Measurement, and Phenomena **14**, 602–605 (1996).

[80] B. J. Rodriguez et al., "Dual-frequency resonance-tracking atomic force microscopy", Nanotechnology **18**, 475504 (2007).

[81] S. Jesse et al., "Direct imaging of the spatial and energy distribution of nucleation centres in ferroelectric materials", Nature Materials **7**, 209–215 (2008).

[82] S. Jesse, A. P. Baddorf, and S. V. Kalinin, "Switching spectroscopy piezoresponse force microscopy of ferroelectric materials", Appl. Phys. Lett. **88**, 062908, 062908 (2006).

[83] A. H. Vlooswijk, "Structure and domain formation in ferroelectric thin films", PhD thesis (University of Groningen, 2009).

[84] C. Lichtensteiger, "InteractiveXRDFit: a new tool to simulate and fit X-ray diffractograms of oxide thin films and heterostructures", J Appl Crystallogr **51**, 1745–1751 (2018).

[85] S. L. Morelhão and J. K. Domagala, "Hybrid reciprocal space for X-ray diffraction in epitaxic layers", J Appl Cryst **40**, 546–551 (2007).

[86] C.-B. Eom, "Synthesis and properties of high T_c superconducting thin films and multilayers grown in situ by 90° off-axis sputtering", PhD thesis (Stanford University, 1991).

[87] C. Lichtensteiger, "Ferroelectricity at the nanoscale: study of size effects in lead titanate thin films", PhD thesis (Université de Genève, 2006).

[88] C. Weymann et al., "Full control of polarisation in ferroelectric thin films using growth temperature to modulate defects", Manuscript in preparation.

[89] S. Gottschalk et al., "Oxygen vacancy kinetics in ferroelectric $PbZr_{0.4}Ti_{0.6}O_3$", Journal of Applied Physics **104**, 114106 (2008).

[90] R. V. K. Mangalam et al., "Unexpected crystal and domain structures and properties in compositionally graded $pbzr_{1-x}ti_xo_3$ thin films", Advanced Materials **25**, 1761–1767 (2013).

[91] M. Mayer, "SIMNRA user's guide", Report IPP **9**, 67 (1997).

[92] S. M. Selbach et al., "PbO-deficient $PbTiO_3$: Mass transport, structural effects and possibility for intrinsic screening of the ferroelectric polarization", Applied Physics Letters **98**, 091912 (2011).

[93] G. H. Dai et al., "A study of Pb vacancies and Pb-O vacancy pairs in doped $Pb_{0.85}Sr_{0.15}$ $(Zr_{0.55}Ti_{0.45})O_3$ ceramics by positron annihilation", J Mater Sci: Mater Electron **2**, 164–170 (1991).

[94] A. Chandrasekaran, "Experimental and first-principles study of point defects, domain walls, and point-defect/domain-wall interactions in ferroelectric oxides", PhD thesis (École polythechnique fédérale de Lausanne, 2015).

[95] Y. Yao and H. Fu, "Charged vacancies in ferroelectric $PbTiO_3$: Formation energies, optimal Fermi region, and influence on local polarization", Phys. Rev. B **84**, 064112 (2011).

[96] G. B. Stephenson and M. J. Highland, "Equilibrium and stability of polarization in ultrathin ferroelectric films with ionic surface compensation", Phys. Rev. B **84**, 064107 (2011).

[97] A. R. Damodaran et al., "Enhancement of ferroelectric curie temperature in $BaTiO_3$ films via strain-induced defect dipole alignment", Advanced Materials **26**, 6341–6347 (2014).

[98] M. Takeda and J. Suzuki, "Crystallographic heterodyne phase detection for highly sensitive lattice-distortion measurements", J. Opt. Soc. Am. A **13**, 1495–1500 (1996).

[99] M. Hÿtch, E. Snoeck, and R. Kilaas, "Quantitative measurement of displacement and strain fields from HREM micrographs", Ultramicroscopy **74**, 131–146 (1998).

[100] E. H. Smith et al., "Hybrid reflections from multiple x-ray scattering in epitaxial oxide films", Appl. Phys. Lett. **111**, 131903 (2017).

[101] G. Catalan et al., "Strain gradients in epitaxial ferroelectrics", Physical Review B **72**, 020102 (2005).

[102] A. M. Glazer and S. A. Mabud, "Powder profile refinement of lead zirconate titanate at several temperatures. II. Pure $PbTiO_3$", Acta Cryst. B **34**, 1065–1070 (1978).

[103] E. Cockayne and B. P. Burton, "Dipole moment of a Pb-O vacancy pair in $PbTiO_3$", Phys. Rev. B **69**, 144116 (2004).

[104] N. Setter et al., "Ferroelectric thin films: Review of materials, properties, and applications", Journal of Applied Physics **100**, 051606 (2006).

[105] P. Zubko et al., "Interface physics in complex oxide heterostructures", Annual Review of Condensed Matter Physics **2**, 141–165 (2011).

[106] S. D. Ha and S. Ramanathan, "Adaptive oxide electronics: A review", Journal of Applied Physics **110**, 071101 (2011).

[107] C. B. Eom et al., "Fabrication and properties of epitaxial ferroelectric heterostructures with ($SrRuO_3$) isotropic metallic oxide electrodes", Appl. Phys. Lett. **63**, 2570–2572 (1993).

[108] C. Lichtensteiger and J.-M. Triscone, "Investigation of ferroelectricity in ultrathin $PbTiO_3$ films", Integrated Ferroelectrics **61**, 143–148 (2004).

[109] M. Dawber et al., "Unusual behavior of the ferroelectric polarization in $PbTiO_3$/$SrTiO_3$ superlattices", Phys. Rev. Lett. **95**, 177601 (2005).

[110] J. Park et al., "Domain alignment within ferroelectric/dielectric $PbTiO_3$/$SrTiO_3$ superlattice nanostructures", Nanoscale **10**, 3262–3271 (2018).

[111] G. Rijnders et al., "Imposed layer-by-layer growth with pulsed laser interval deposition", Applied Surface Science, Special Issue: Proceedings of the European Materials Research **168**, 223–226 (2000).

[112] C. Weymann et al., "Improved thin film growth using Slow Kinetics Intermittent Sputtering", Applied Surface Science **516**, 146077 (2020).

[113] R. K. Behera et al., "Structure and energetics of 180° domain walls in $PbTiO_3$ by density functional theory", J. Phys.: Condens. Matter **23**, 175902 (2011).

[114] A. Kiselev et al., "Active sites in heterogeneous ice nucleation—the example of K-rich feldspars", Science **355**, 367–371 (2017).

[115] N. Domingo et al., "Surface charged species and electrochemistry of ferroelectric thin films", Nanoscale **11**, 17920–17930 (2019).